Quantum reactive scattering in three dimensions using hyperspherical (APH) coordinates. IV. Discrete variable representation (DVR) basis functions and the analysis of accurate results for $F+H_2$

Z. Bačić,[a] J. D. Kress, G. A. Parker,[b] and R. T Pack
Theoretical Division (T-12, MS J569), Los Alamos National Laboratory, Los Alamos, New Mexico 87545

(Received 18 September 1989; accepted 10 November 1989)

Accurate 3D coupled channel calculations for total angular momentum $J = 0$ for the reaction $F + H_2 \rightarrow HF + H$ using a realistic potential energy surface are analyzed. The reactive scattering is formulated using the hyperspherical (APH) coordinates of Pack and Parker. The adiabatic basis functions are generated quite efficiently using the discrete variable representation method. Reaction probabilities for relative collision energies of up to 17.4 kcal/mol are presented. To aid in the interpretation of the resonances and quantum structure observed in the calculated reaction probabilities, we analyze the phases of the S matrix transition elements, Argand diagrams, time delays and eigenlifetimes of the collision lifetime matrix. Collinear (1D) and reduced dimensional 3D bending corrected rotating linear model (BCRLM) calculations are presented and compared with the accurate 3D calculations.

I. INTRODUCTION

The reaction

$$F + H_2 \rightarrow HF + H, \quad (1)$$

has been the subject of much activity, both experimental and theoretical, in an attempt to understand the state-to-state dynamics of this highly exothermic process. On the experimental side, both chemical laser[1] and infrared chemiluminescence[2] studies have measured the product vibrational state distributions. At thermal energies, the $v = 2$ and 3 distributions of vibrationally excited products $HF(v)$ are highly inverted with respect to the $v = 0$ and 1 distributions. More recently, Lee and co-workers[3] have used molecular beam techniques to measure the differential cross sections (DCSs) for relative collision energies (E_{rel}) of 0.7–3.4 kcal/mol. The DCSs for $v = 1$ and 2 exhibited mostly backwards scattering, whereas in the DCS for $v = 3$ substantial forward scattering was observed at all energies studied. They concluded from the $v = 3$ results that dynamical resonances play a significant role in the reaction.

Central to any theoretical treatment (classical or quantum) of the reaction dynamics is an accurate description of the potential energy surface (PES). Numerous dynamical studies have been performed using surface No. 5 of Muckerman,[4] which is denoted M5. Resonances for the $F + H_2$ reaction were first observed in collinear (1D) quantum scattering calculations[5] using the M5 PES. Subsequently, many approximate 3D quantum scattering calculations using distorted wave,[6] centrifugal sudden[7] (CS), infinite order sudden[8] (IOS), and bending corrected rotating linear model[9] (BCRLM) techniques have been carried out using the M5 PES. More recently, full 3D variational calculations for zero total angular momentum ($J = 0$) have been reported by both Zhang and Miller[10] and Yu *et al.*[11] employing the M5 surface.

Unfortunately, the M5 PES is known to have deficiencies in terms of explaining the experimental observation[3] both of dynamical resonances and the lack of a delayed threshold for producing $v = 3$ products. In an attempt to improve upon the threshold behavior of the M5 PES, Truhlar and co-workers have developed a series of PESs[12–15] which were adjusted through the use of both *ab initio* electronic structure calculations and variational transition state calculations of the $v = 3$ and total reactivity thresholds. Although they are continuing to develop improved versions, Truhlar and co-workers[16] believe that the surface No. 5A (Ref. 13 as modified in Ref. 14) should be accurate enough to correctly predict some of the major observations of the experiment. This surface, which we denote as T5A, is the PES employed in the present calculations. Some indication of the accuracy of the T5A PES has been provided by the BCRLM calculations of Hayes and Walker[9]; their DCSs agree much better with experiment[3] than those calculated with other PESs. However, the BCRLM results for the T5A PES do not provide adequate explanations for all of the observed resonance effects, and it is not clear how much of this is due to the BCRLM approximation and how much is due to the T5A PES.

Very recently accurate 3D coupled channel (CC) calculations using the T5A PES have appeared. In Ref. 17, we presented $J = 0$ reaction probabilities for relative collision energies of E_{rel} up to 17.4 kcal/mol. Variational calculations for $J = 0$ on the T5A PES have been reported by Yu *et al.*[16,18] for E_{rel} up to 3.5 kcal/mol. Reference 18 also contains $J = 1$ results for E_{rel} up to 3.4 kcal/mol and a $J = 2$ calculation for $E_{rel} = 1.84$ kcal/mol.

In this article an in-depth analysis is provided of the calculations first reported in Ref. 17. Details are given on the application of the discrete variable representation (DVR) method[19] for calculating adiabatic basis (surface) functions

[a] Present and permanent address: Department of Chemistry, New York University, New York, NY 10003.
[b] Present and permanent address: Department of Physics and Astronomy, University of Oklahoma, Norman, OK 73019.

 0021-9606/90/042344-18$03.00

needed in the adiabatically adjusting principal axis hyperspherical (APH) theory[20] of reactive scattering. The finite element method (FEM), which was used in earlier calculations for the reactions $H + H_2$ and $D + H_2$,[20,21] proved to be too slow and too inaccurate for the $F + H_2$ system. (However, since the completion of this work a different diagonalization routine, the spectral transform Lanczos method[22] (STLM), has been added to the FEM code. Preliminary calculations[23] show the STLM to be much more efficient than the previous subspace iteration diagonalization method. At this time, it is not clear how the FEM-STLM will compare to the DVR method in terms of both speed and accuracy.)

The rest of this article is organized as follows. In Sec. II, the APH scattering theory is briefly reviewed and the details of the DVR method are presented. In Sec. III, the convergence of the surface function basis with respect to the DVR parameters is discussed and the production run parameters are specified. Section IV contains the present results, which include a correlation diagram, reaction probabilities, phase plots, time delays and the eigenvalues of the collision lifetime matrix. In Sec. V, the results are discussed and the resonances are analyzed. Section VI contains the conclusions.

II. THEORY

A. APH scattering formalism

The reactive scattering for the three atom system is formulated using the APH theory, which is detailed in Ref. 20. In this section a brief sketch is given of the details necessary for understanding the application of the DVR method to the surface function problem.

The total scattering wave function is expanded [Eq. (70) in Ref. 20] in a set of solutions Ψ^{JMpi}, which are regular at the origin. J is the total angular momentum quantum number, M is the quantum number for the projection of J along the space frame z axis, p is the parity and i represents the ith solution. Each Ψ^{JMpi} is expanded in a sector adiabatic basis $\Phi^{Jp}_{t\Lambda}(\theta,\chi;\rho_\xi)$ as

$$\Psi^{JMpi} = 4\sum_{t,\Lambda} \rho^{-5/2}\psi^{Jpi}_{t\Lambda}(\rho)\Phi^{Jp}_{t\Lambda}(\theta,\chi;\rho_\xi)\hat{D}^{Jp}_{\Lambda M}(\alpha_Q,\beta_Q,\gamma_Q), \tag{2}$$

where ρ is the APH hyperradius and θ and χ are the APH hyperangles. ρ_ξ is the center of a sector, where the range of ρ is divided into n sectors, $\xi = 1,...,n$. The expansion coefficients $\psi^{Jpi}_{t\Lambda}(\rho)$ are radial wave functions. The $\hat{D}^{Jp}_{\Lambda M}(\alpha_Q,\beta_Q,\gamma_Q)$ are normalized[20] Wigner rotation matrix elements of good parity p which are a function of the APH Euler angles.

For each ρ_ξ, the surface functions for $J = 0$ satisfy the 2D Schrödinger equation

$$\left\{-\frac{\hbar^2}{2\mu\rho_\xi^2}\left[\frac{4}{\sin 2\theta}\frac{\partial}{\partial\theta}\sin 2\theta\frac{\partial}{\partial\theta} + \frac{1}{\sin^2\theta}\frac{\partial^2}{\partial\chi^2}\right] + \frac{15\hbar^2}{8\mu\rho_\xi^2} + V(\rho_\xi,\theta,\chi) - \mathscr{E}^{J=0,p}_{t,\Lambda=0}(\rho_\xi)\right\}\Phi^{J=0,p}_{t,\Lambda=0}(\theta,\chi;\rho_\xi) = 0, \tag{3}$$

where μ is the three atom reduced mass and V is the interaction potential. In this work we consider only solutions of even parity $p = 0$, and we are scattering only out of initial H_2 states of even j rotational quantum numbers. In the following discussions the $J = 0, p = 0$ and $\Lambda = 0$ indices from both Φ and $\mathscr{E}$ will be suppresed.

When the APH wave function of Eq. (2) is substituted into the full Schrödinger equation [Eq. (61) in Ref. 20] for $J = 0$, a set of N coupled channel (CC) equations [Eq. (65) in Ref. 20] is obtained, where N is the number of surface functions in the CC expansion. These exact CC equations are propagated from ρ_1 to ρ_n using the log-derivative method,[24] and at ρ_n the boundary conditions are applied as specified in Ref. 20.

B. The DVR method

For each ρ_ξ, $\xi = 1,...,n$, the bound state solutions $\Phi_t(\theta,\chi;\rho_\xi)$ to Eq. (3) must be found. This is often the most time consuming part of the APH calculations for two reasons. First, a large number of surface functions (N) have to be calculated for each of a large number (n) of values of ρ_ξ. For $F + H_2$, we use up to $N = 150$ and $n = 147$. Second, the potential is highly nonseparable in θ and χ; its shape and value vary strongly with ρ. Thus, having a fast, accurate and very flexible method for calculating highly excited bound states of arbitrarily shaped multidimensional (in this case, two-dimensional) potentials is essential for the feasibility of APH calculations.

Bound state methods using localized representations, the discrete variable representation (DVR)[19] and distributed Gaussian bases (DGB),[25] have been recently developed by Bačić, Light, and co-workers.[26,27] They have been shown to be exceptionally effective for calculating the high-lying, large amplitude vibrational states of such challenging triatomic systems as LiCN/LiNC,[28,29] HCN/HNC,[29,30] H_2O,[31] and H_3^+.[32] This fact, and the successful DVR surface function calculation for $H + H_2$,[33] have motivated us to apply this approach to $F + H_2$.[17,34] We use the DVR for the calculation of surface functions and the various matrix elements involving the surface functions which are required for the CC scattering calculations.

1. 2D DVR calculation of surface functions

To obtain the surface functions Φ_t in Eq. (3), the approach of Whitnell and Light[33] is adopted, in which the DVR is used for both θ and χ; the surface functions are determined using the sequential diagonalization-truncation procedure of Bačić, Light *et al.*[26–33] In this approach, the surface function Hamiltonian matrix is first formed (formally at least) in the direct product finite basis representation (FBR); it is subsequently transformed to the DVR.[19,26–33] The FBR employed in this work consisted of (normalized) Legendre polynomials in $\cos 2\theta$, $\{\hat{P}_l(\cos 2\theta), l = 0,1,...,l_{\max}\}$, for the θ coordinate, and of a set of symmetry adapted (normalized) trigonometric functions $\{\Pi_m(\chi), m = 1,2,...,m_{\max}\}$

$$\Pi_m(\chi) = \left(\frac{1+\delta_{m,1}}{\pi}\right)^{1/2}\cos 2(m-1)\chi, \tag{4}$$

for the χ coordinate.[33] Thus, in this direct product FBR, the surface functions Φ_t could be written as

$$\Phi_t = \sum_{l=0}^{l_{\max}} \sum_{m=1}^{m_{\max}} k_{lm}^t \hat{P}_l(\cos 2\theta)\Pi_m(\chi). \tag{5}$$

As discussed by Whitnell and Light,[33] a minor modification of the 2D surface function Schrödinger equation [Eq. (3)] was required before the Legendre polynomials could be used as the FBR for θ. A coordinate

$$\theta' = 2\theta \tag{6}$$

was defined, which resulted in the surface function Schrödinger equation[33]

$$\left\{ -\frac{\hbar^2}{2\mu\rho_\xi^2}\left[\frac{16}{\sin\theta'}\frac{\partial}{\partial\theta'}\sin\theta'\frac{\partial}{\partial\theta'} + \frac{1}{\sin^2(\theta'/2)}\frac{\partial^2}{\partial\chi^2}\right] + \tilde{V}(\rho_\xi,\theta',\chi)\right\}\Phi_t = \mathscr{E}_t\Phi_t. \tag{7}$$

The symbol $\tilde{V}$ in Eq. (7) stands for

$$\tilde{V}(\rho_\xi,\theta',\chi) = V(\rho_\xi,\theta',\chi) + \frac{15\hbar^2}{8\mu\rho_\xi^2}. \tag{8}$$

[This is why $\cos 2\theta$ appears in the argument of the P_l's in the definition of the FBR before Eq. (4).] From now on, θ will no longer be primed, but it should be understood that it is defined by Eq. (6). Let us now define

$$h_\theta = -\frac{\hbar^2}{2\mu\rho_\xi^2}\frac{16}{\sin\theta}\frac{\partial}{\partial\theta}\sin\theta\frac{\partial}{\partial\theta}, \tag{9}$$

$$h_\chi = -\frac{\hbar^2}{2\mu\rho_\xi^2}\frac{\partial^2}{\partial\chi^2}, \tag{10}$$

and

$$f_\theta = \left[\sin\left(\frac{\theta}{2}\right)\right]^{-2}. \tag{11}$$

With the above definitions, Eq. (7) can be rewritten as

$$[(h_\theta + f_\theta h_\chi) + \tilde{V}(\rho_\xi,\theta,\chi)]\Phi_t = \mathscr{E}_t\Phi_t. \tag{12}$$

The FBR-DVR transformation matrices and points for θ and χ were obtained by diagonalizing the coordinate matrices in the corresponding FBR basis. For θ, $\cos\theta$ was diagonalized in the $\{\hat{P}_l(\cos\theta)\}$ basis. The eigenvalues were the θ DVR points, while the eigenvectors formed the FBR-DVR transformation matrix[19] $\mathbf{T}^\theta$ for the θ coordinate. A symmetry adapted DVR[33] (SADVR) was formed for χ. The SADVR in χ was constructed from the eigenvalues of the matrix of $\cos 2\chi$ formed in the $\{\Pi_m(\chi)\}$ basis defined by Eq. (4). As in the case of θ, the eigenvectors of this matrix formed the FBR-DVR transformation matrix for χ, $\mathbf{T}^\chi$. The full 2D FBR-DVR transformation matrix for (θ,χ), $\mathbf{T}$, is the direct product of the 1D transformation matrices $\mathbf{T}^\theta$ and $\mathbf{T}^\chi$,

$$\mathbf{T} = \mathbf{T}^\chi \otimes \mathbf{T}^\theta. \tag{13}$$

The DVR representation of the surface function Hamiltonian is obtained as

$$\mathbf{H}^{\mathrm{DVR}} = \mathbf{T}^T\mathbf{H}^{\mathrm{FBR}}\mathbf{T}, \tag{14}$$

where $\mathbf{H}^{\mathrm{FBR}}$ is the matrix representation of the surface Hamiltonian in Eq. (12) formed in the FBR defined in Eq. (5), and $\mathbf{T}$ is defined in Eq. (13). With the help of symbols defined in Eqs. (9)–(11), Eq. (14) can be written as

$$\mathbf{H}^{\mathrm{DVR}} = \mathbf{h}_\theta^{\mathrm{DVR}} \otimes \mathbf{I}_\chi + \mathbf{f}_\theta^{\mathrm{DVR}} \otimes \mathbf{h}_\chi^{\mathrm{DVR}} + \tilde{\mathbf{V}}^{\mathrm{DVR}}, \tag{15}$$

where $\mathbf{I}_\chi$ is the unit matrix on the χ basis,

$$\mathbf{h}_x^{\mathrm{DVR}} = \mathbf{T}^T\mathbf{h}_x\mathbf{T}, \quad (x = \theta,\chi) \tag{16}$$

$$\tilde{V}_{\alpha'\beta',\alpha\beta}^{\mathrm{DVR}} = \tilde{V}(\rho_\xi,\theta_\alpha,\chi_\beta)\delta_{\alpha'\alpha}\delta_{\beta'\beta}, \tag{17}$$

and

$$f_{\theta,\alpha'\alpha}^{\mathrm{DVR}} = \left[\sin\left(\frac{\theta_\alpha}{2}\right)\right]^{-2}\delta_{\alpha'\alpha}. \tag{18}$$

Equations (17) and (18) are due to the fact that in the DVR, operators representing functions are diagonal[19,26–33]; $\mathbf{f}_\theta^{\mathrm{DVR}}$ and $\tilde{\mathbf{V}}^{\mathrm{DVR}}$ are simply evaluated at the corresponding quadrature points.

The surface functions Φ_t could now be obtained by directly diagonalizing $\mathbf{H}^{\mathrm{DVR}}$ of Eq. (15). However, the sequential diagonalization-truncation technique[26–33] can reduce drastically the dimension of $\mathbf{H}^{\mathrm{DVR}}$, and therefore the computational effort associated with its diagonalization. As done by Whitnell and Light,[33] for each θ_α, $\alpha = 1,2,\ldots, l_{\max}+1$, a 1D ray Hamiltonian[26–33] in χ is formed:

$$H_{\alpha'\alpha,\beta'\beta}^{\mathrm{1D}} = (h_\chi^{\mathrm{DVR}})_{\beta'\beta}(f_\theta^{\mathrm{DVR}})_{\alpha'\alpha}\delta_{\alpha'\alpha} + \tilde{V}_{\alpha'\alpha,\beta'\beta}^{\mathrm{DVR}}\delta_{\alpha'\alpha}\delta_{\beta'\beta}. \tag{19}$$

Prior to its diagonalization, the 1D ray Hamiltonian in Eq. (19) was truncated by keeping only those DVR quadrature points satisfying the potential energy cutoff

$$V(\rho_\xi,\theta_\alpha,\chi_\beta) \leqslant V_{\max}. \tag{20}$$

Diagonalization of the (truncated) 1D ray Hamiltonian in Eq. (19)

$$(\mathbf{d}^\alpha)^T\mathbf{H}^{\mathrm{1D}}\mathbf{d}^\alpha = {}^{\mathrm{1D}}\mathbf{E}^\alpha, \tag{21}$$

yields the matrix of 1D ray eigenvectors, $\mathbf{d}^\alpha$, and the diagonal matrix ${}^{\mathrm{1D}}\mathbf{E}^\alpha$, containing the ray eigenvalues. The dimensions of both matrices were $N_\chi^\alpha \times N_\chi^\alpha$, where N_χ^α is the number of χ DVR points retained on the cut defined by $\cos\theta_\alpha$. $\mathbf{d}^\alpha$ was truncated by retaining those 1D ray eigenvectors whose eigenvalues ${}^{\mathrm{1D}}E_p^\alpha$ satisfied the energy cutoff condition

$${}^{\mathrm{1D}}E_p^\alpha \leqslant E_{\mathrm{cut}}. \tag{22}$$

The truncated $\mathbf{d}^\alpha$ is an $N_\chi^\alpha \times n_\alpha$ matrix, with n_α being the number of ray eigenvalues retained on the ray $\cos\theta_\alpha$.

In the final step, $\mathbf{H}^{\mathrm{DVR}}$, the 2D DVR surface Hamiltonian in Eq. (15), is transformed to the 1D (truncated) χ ray eigenvector basis.[26–33] The general α,α' block of the surface Hamiltonian matrix in the ray eigenvector basis, $\tilde{\mathbf{H}}^{\mathrm{DVR}}$, is obtained as

$$\tilde{\mathbf{H}}^{\mathrm{DVR}\alpha\alpha'} = (\mathbf{d}^\alpha)^T\mathbf{H}^{\mathrm{DVR}\alpha\alpha'}\mathbf{d}^{\alpha'}, \tag{23}$$

where $\mathbf{H}^{\mathrm{DVR}\alpha\alpha'}$ is the α,α' block of $\mathbf{H}^{\mathrm{DVR}}$ in Eq. (15). The dimensions of $\tilde{\mathbf{H}}^{\mathrm{DVR}\alpha\alpha'}$ are $n_\alpha \times n_{\alpha'}$. Diagonalization of $\tilde{\mathbf{H}}^{\mathrm{DVR}}$ (which is of order $n_{\mathrm{ev}} = \Sigma_\alpha n_\alpha$),

$$\mathbf{C}^T\tilde{\mathbf{H}}^{\mathrm{DVR}}\mathbf{C} = \mathbf{E}^{\mathrm{SF}}, \tag{24}$$

produces the desired surface eigenvalues $\mathscr{E}_t$ in $\mathbf{E}^{\mathrm{SF}}$, while the surface function eigenvectors Φ_t (in the ray eigenvector basis) form the columns of matrix $\mathbf{C}$. Because of the relatively small size ($n_{\mathrm{ev}} < 940$), $\tilde{\mathbf{H}}^{\mathrm{DVR}}$ can be diagonalized directly.

2. DVR calculation of the potential coupling matrix elements and overlap matrices

Let us define $U(\rho_\xi,\rho,\theta,\chi)$ as

$$U(\rho_\xi,\rho,\theta,\chi) = V(\rho,\theta,\chi) - \frac{\rho_\xi^2}{\rho^2} V(\rho_\xi,\theta,\chi). \quad (25)$$

Solving the APH CC equations requires evaluation of the potential coupling matrix elements [see Eq. (168) in Ref. 20] of U,

$$U^{\Phi}_{tt'} = \langle \Phi_t(\theta,\chi;\rho_\xi) | U(\rho_\xi,\rho,\theta,\chi) | \Phi_{t'}(\theta,\chi;\rho_\xi) \rangle, \quad (26)$$

at a few values of ρ about the center ρ_ξ of each sector. Let $\mathbf{U}^{\mathrm{FBR}}$ be the matrix of U in Eq. (25) in the direct product FBR defined in Eq. (5). Then,

$$\mathbf{U}^{\mathrm{DVR}} = \mathbf{T}^T \mathbf{U}^{\mathrm{FBR}} \mathbf{T}, \quad (27)$$

where, to a very good approximation,[19,26]

$$U^{\mathrm{DVR}}_{\alpha'\beta',\alpha\beta} = \delta_{\alpha'\alpha}\delta_{\beta'\beta}\, U(\rho_\xi,\rho,\cos\theta_\alpha,\cos 2(n-1)\chi_\beta). \quad (28)$$

$\mathbf{U}^{\mathrm{DVR}}$ is transformed to the (contracted) 1D ray eigenvector basis in χ, since the surface functions $\{\Phi_t\}$ were determined in that basis. The α,α block of $\mathbf{U}^{\mathrm{DVR}}$ in the ray eigenvector basis, $\tilde{\mathbf{U}}^{\mathrm{DVR}}$, is obtained as

$$\tilde{\mathbf{U}}^{\mathrm{DVR}\alpha\alpha} = (\mathbf{d}^\alpha)^T \mathbf{U}^{\mathrm{DVR}\alpha\alpha} \mathbf{d}^\alpha, \quad (29)$$

where $\mathbf{d}^\alpha$ is the 1D ray eigenvector matrix (calculated at $\cos\theta_\alpha$) defined in Eq. (21). Finally, the potential coupling matrix in the basis of 2D DVR surface functions [Eq. (26)], $\mathbf{U}^{\Phi}$, is obtained as

$$\mathbf{U}^{\Phi} = \mathbf{C}^T \tilde{\mathbf{U}}^{\mathrm{DVR}} \mathbf{C}, \quad (30)$$

where $\mathbf{C}$ is matrix of the surface eigenvectors $\{\Phi_t\}$ (arranged in columns) obtained by diagonalizing $\tilde{\mathbf{H}}^{\mathrm{DVR}}$ in Eq. (24).

The overlap matrix $\mathbf{O}$ between surface functions belonging to neighboring ξ th and $(\xi+1)$st sectors, with elements

$$O_{tt'} = \langle \Phi_t(\rho_\xi) | \Phi_{t'}(\rho_\xi + 1) \rangle, \quad (31)$$

is needed to transform the $\mathbf{R}$ matrix from one sector to the next.[20] Since the 1D ray eigenvector bases in χ used for calculating the Φ_t's at ρ_ξ and $\rho_{\xi+1}$ are different, the surface functions had to be transformed to the (primitive, uncontracted) 2D DVR, which was the same for all ρ values.[17] Let an arbitrary element of the t th surface eigenvector Φ_t, stored in the t th column of matrix $\mathbf{C}$ in Eq. (24), be labeled as C^α_{pt}, where $\alpha = 1,2,...,N_\theta = l_{\max}+1$ (order of the θ DVR), and $p = 1,2,...,n_\alpha$ (number of 1D ray eigenvectors in χ, at $\cos\theta_\alpha$, retained in the final basis). Also, let d^α_{mp} be an element of the pth ray eigenvector, stored columnwise in the matrix $\mathbf{d}^\alpha$ of Eq. (21), where $m = 1,2,...,N_\chi = m_{\max}$ (order of the χ DVR). Then, the t th surface eigenvector in the (primitive) 2D DVR, with elements ϕ^α_{mt} $(m = 1,2,...,N_\chi)$, is obtained via

$$\phi^\alpha_{mt} = \sum_{p=1}^{n_\alpha} d^\alpha_{mp} C^\alpha_{pt} \quad (\alpha = 1,2,...,N_\theta). \quad (32)$$

The overlap matrix elements $O_{tt'}$ in Eq. (31) are given by

$$O_{tt'} = \sum_{\alpha=1}^{N_\theta} \sum_{m=1}^{N_\chi} \phi^\alpha_{mt} \phi^\alpha_{mt'}. \quad (33)$$

3. Transformation of surface functions from 2D DVR to FBR

To apply the boundary conditions at ρ_n (to obtain the Delves $\mathbf{R}$ matrix from the APH $\mathbf{R}$ matrix), the surface functions in the 2D DVR must be transformed to the FBR in Eq. (5).

Transformation of a surface eigenvector in the (primitive) 2D DVR, with elements ϕ^α_{mt} [Eq. (32)], to the FBR in χ is accomplished by

$$[g^\alpha_m]_t = \sum_{i=1}^{N_\chi} T^\chi_{mi} \phi^\alpha_{it}, \quad (34)$$

where T^χ_{mi} are the elements of the 1D FBR-DVR transformation matrix $\mathbf{T}^\chi$. The elements $[g^\alpha_m]_t$ appearing in Eq. (34), are now expansion coefficients in the χ FBR basis set $\{\Pi_m(\chi)\}$ defined in Eq. (4),

$$[f^\alpha(\chi)]_t = \sum_{m=1}^{N_\chi} [g^\alpha_m]_t \Pi_m(\chi). \quad (35)$$

The FBR expansion of Φ_t in Eq. (5) can be written as

$$\Phi_t = \sum_{l=0}^{l_{\max}} [f_l(\chi)]_t \hat{P}_l(\cos\theta), \quad (36)$$

where

$$[f_l(\chi)]_t = \sum_{m=1}^{m_{\max}} k^t_{lm} \Pi_m(\chi). \quad (37)$$

Transformation of the $[f^\alpha]_t$'s in Eq. (35) to the $[f_l]_t$'s which appear in Eq. (36) is achieved by

$$[f_l(\chi)]_t = \sum_{\alpha=1}^{N_\theta} T^\theta_{l\alpha} [f^\alpha(\chi)]_t. \quad (38)$$

Elements $T^\theta_{l\alpha}$ in Eq. (38) belong to the 1D FBR-DVR transformation matrix $\mathbf{T}^\theta$. If Eq. (35) is inserted into Eq. (38), one obtains

$$[f_l(\chi)]_t = \sum_{m=1}^{N_\chi} \sum_{\alpha=1}^{N_\theta} T^\theta_{l\alpha} [g^\alpha_m]_t \Pi_m(\chi). \quad (39)$$

By comparing the two expressions for $[f_l(\chi)]_t$, in Eqs. (37) and (39), respectively, it is easily found that the expansion coefficients are

$$k^t_{lm} = \sum_{\alpha=1}^{N_\theta} T^\theta_{l\alpha} [g^\alpha_m]_t = \sum_{\alpha=1}^{N_\theta} \sum_{i=1}^{N_\chi} T^\theta_{l\alpha} T^\chi_{mi} \phi^\alpha_{it}. \quad (40)$$

III. SURFACE FUNCTION CONVERGENCE AND PARAMETERS

A. Convergence

In this section the convergence of the DVR surface functions with respect to the DVR parameters is examined and the actual parameters used in the production run are specified. For the scattering calculations, $n = 147$ sectors were used where $\rho_1 = 2.2\ a_0$ and $\rho_n = 9.405\ a_0$. ($1\ a_0 = 1$ bohr unit). Since the topology of the potential varies significantly as ρ changes from ρ_1 to ρ_n, convergence was verified at several representative values of ρ. (See Ref. 35 for perspec-

tive plots of the stereographic projection of the T5A potential in θ and χ for $\rho = 5.2$ and 7.3 a_0). To apply the DVR most efficiently, different values of l_{max} and m_{max} should be used on different subintervals within the basic interval $[\rho_1,\rho_n]$. As will be demonstrated by the convergence studies, smaller FBRs can be used at small values of ρ where the amplitude of the surface functions tends to be delocalized in θ and χ. As ρ increases and the asymptotic arrangement channel limit is approached, the surface functions localize in each arrangement channel and only limited regions of θ and χ contain amplitude. In this case larger FBRs must be used which in turn define DVRs which place more grid points in these limited regions of APH hyperangle space. In future applications of the DVR, we plan to adjust l_{max} and m_{max} as a function of ρ. However, in this initial application, to avoid calculating overlap matrices between surface functions defined with different l_{max} and m_{max} values, a single set of (l_{max},m_{max}) was used which converged the surface functions at ρ_n. This choice provides a more than adequate basis in terms of l_{max} and m_{max} for all ρ due to the reasons discussed above.

In Table I some of the convergence tests which were performed are summarized. The focus of this study is surface functions $t = 98$–100. The states $t < 100$ are as converged or better converged than the $t = 100$ state although some exceptions occur. States $t = 98$–100 are representative of the three types of surface functions which are encountered in the $F + H_2$ problem. In general, states which correlate asymptotically with H_2, [such as $t = 100$, a $(v = 1, j = 0)$ state at 2.159 eV], converge much more quickly than those which correlate with HF. Also, states which correlate with HF ($j = large$), [such as $t = 99$], converge much more slowly than those which correlate with HF ($j = small$), [such as $t = 98$]. This last difference is due mainly to the fact that large j functions contain many nodes in the direction of rotational motion and require more grid points to reproduce. (Plots of surface functions for $F + H_2$ which correlate asymptotically with a H_2, a HF ($v = 3, j = small$), and a HF ($v = 2, j = large$) state are shown in Ref. 35.) Fortunately, the HF ($j = large$) states receive very little flux, so their convergence is less important. It is important, though, to be aware of these convergence properties. One can be misled in a convergence study if only one particular state is focussed upon and this state turns out to be more slowly or quickly converging than the other states of interest. This is why in Table I three consecutive states are considered. Actually, all of the surface function energies are analyzed to assure convergence although it is not practical to present all of the results.

TABLE I. Surface function eigenvalues $\mathscr{E}_t(\rho)$.

l_{max}	m_{max}	n_{ev}	V_{max} (eV)	E_{cut} (eV)	$\mathscr{E}_t(\rho = 2.2\ a_0)$ (eV) $t = 98$	$t = 99$	$t = 100$
25	40	501	30.0	25.0	14.1273	14.1581	14.2141
25	40	409	30.0	21.0	14.1288	14.1582	14.2151
25	40	381	30.0	20.0	14.1291	14.1583	14.2160
25	40	246	30.0	15.0	14.1970	14.2150	14.2751
25	40	381	35.0	20.0	14.1291	14.1583	14.2160
25	30	454	30.0	25.0	14.1663	14.2145	14.2571
25	50	517	30.0	25.0	14.1277	14.1582	14.2142
25	60	519	30.0	25.0	14.1278	14.1582	14.2142
30	40	594	30.0	25.0	14.1274	14.1605	14.2158
35	40	689	30.0	25.0	14.1326	14.1624	14.2189
50	100	885	39.4	22.5	14.1299	14.1686	14.2191
					$\mathscr{E}_t(\rho = 3.038\ a_0)$ (eV)		
25	40	532	20.0	10.0	4.534 23	4.543 38	4.548 93
25	40	596	20.0	12.0	4.534 17	4.543 37	4.548 88
25	50	551	20.0	10.0	4.542 33	4.546 16	4.548 40
25	60	552	20.0	10.0	4.542 30	4.546 03	4.548 41
30	50	652	20.0	10.0	4.542 89	4.546 62	4.548 84
50	100	886	14.0	8.0	4.544 64	4.547 27	4.552 55
					$\mathscr{E}_t(\rho = 4.975\ a_0)$ (eV)		
30	50	541	7.0	4.0	2.164 87	2.180 24	2.189 30
30	60	546	7.0	4.0	2.164 51	2.179 88	2.189 32
40	60	721	7.0	4.0	2.164 51	2.179 86	2.189 32
40	60	598	7.0	3.5	2.164 84	2.180 80	2.189 51
50	100	897	7.0	4.0	2.164 51	2.179 85	2.189 32
					$\mathscr{E}_t(\rho = 9.5\ a_0)$ (eV)		
50	80	465	7.0	4.0	2.153 02	2.154 65	2.155 13
50	90	488	7.0	4.0	2.142 06	2.155 07	2.155 50
50	120	507	7.0	4.0	2.150 58	2.155 03	2.155 21
40	100	406	7.0	4.0	2.154 71	2.155 28	2.158 61
60	100	406	7.0	4.0	2.149 93	2.155 04	2.155 57
70	100	703	7.0	4.0	2.149 86	2.155 07	2.155 65
50	100	506	6.0	4.0	2.148 74	2.154 98	2.155 17
50	100	472	7.0	3.8	2.148 92	2.155 03	2.155 47
50	100	506	7.0	4.0	2.148 71	2.154 98	2.155 17

1. Convergence at $\rho = 2.2$ and 3.038 a_0

There are four DVR parameters, l_{max}, m_{max}, V_{max}, and E_{cut}, which must be determined. First, the surface functions at the initial value of $\rho_1 = 2.2\ a_0$ are considered in Table I. For fixed values of l_{max} and m_{max}, $E_{cut} = 20.0$ eV and $V_{max} = 30.0$ eV provide at least four figures of convergence. For fixed values of E_{cut} and V_{max}, $l_{max} = 30$ and $m_{max} = 50$ provide at least four figures of convergence. A general property which can signal convergence with respect to m_{max} is observed here. Eventually a change in m_{max} produces a nearly zero change in the order n_{ev} of the 2D DVR surface Hamiltonian matrix. This is due to the order of application of the DVRs; we take fixed θ values and define 1D DVRs in χ.

Next in Table I convergence results for $\rho = 3.038$ eV are presented. Note how much the energies have dropped with respect to those at $\rho = 2.2\ a_0$. This drop in energy allows for the use of a smaller value of E_{cut}. As apparent in Table I, $E_{cut} = 10.0$ eV, $l_{max} = 25$, and $m_{max} = 50$ provide at least four

figures of convergence. One compromise must be made when using values of l_{max} and m_{max} larger than the optimal values: E_{cut} must be set at less than its optimal value. This keeps the value of n_{ev} down to a reasonable size which is necessary as the computational work to diagonalize the 2D DVR matrix scales as $(n_{ev})^3$. By setting $E_{cut} = 8.0$ eV, down from the optimal 10.0 eV, a deviation of up to 0.004 eV is introduced in the states in Table I. Yet it appears that this compromise does not affect the quality of the final scattering results as we show later. This possibly suggests that requirement of four figure convergence for the $t = 100$ surface function at *all* values of ρ is a bit conservative.

2. Convergence at $\rho = 4.975$ and 9.5 a_0

In Table I next are the results for $\rho = 4.975\ a_0$. By comparing these energies with those listed for $\rho = 9.5\ a_0$ we see that at $\rho \approx 5.0\ a_0$ the surface function energies are roughly the same as those at the asymptotic limit. $E_{cut} = 4.0$ eV, $l_{max} = 30$ and $m_{max} = 60$ provide at least four figures of convergence. Since the surface function energies are nearly at their asymptotic values, $E_{cut} = 4.0$ eV was used for values of $\rho > 5.0\ a_0$.

Finally, convergence results for $\rho = 9.5\ a_0$ are presented in Table I. $E_{cut} = 4.0$ eV, $V_{max} = 7.0$ eV, $l_{max} = 50$ and $m_{max} = 100$ provide at least four figures of convergence for states $t = 99$ and 100. State $t = 98$ exhibits properties that correlate with an HF $(v, j = large)$ state. Although the size of the 2D DVR matrix for $m_{max} = 100$ is nearly stationary with respect to the $m_{max} = 120$ matrix ($n_{ev} = 506$ vs $n_{ev} = 507$), the $t = 98$ energy is converged to only ≈ 0.002 eV with respect to m_{max} (varies by 2 in the 4th figure).

B. Parameters

For production runs, values of $l_{max} = 50$, $m_{max} = 100$ and $V_{max} = 1.75\ E_{cut}$ are used. Since the optimal choice for E_{cut} $[\approx 2\mathscr{E}_{t=100}(\rho)]$ is tied to the value of ρ through $\mathscr{E}_{t=100}(\rho)$, E_{cut} is allowed to vary using a linear interpolation scheme for $\rho = [2.2, 4.028]\ a_0$. The interpolation knots are $\rho = 2.2$, 2.518, 2.79, 3.038, 3.553, and 4.028 a_0 with corresponding values of $E_{cut} = 22.5$, 14.8, 10.6, 8.0, 5.2, and 4.0 eV. $E_{cut} = 4.0$ eV for $\rho = [4.028, 9.5]\ a_0$.

Before leaving Table I, consider the variation of n_{ev} as a function of ρ using the production set of DVR parameters. The value of n_{ev} provides some measure of the number of grid points on the θ, χ space where the potential is less than V_{max}. $n_{ev} = 897$ at $\rho = 4.975\ a_0$, whereas $n_{ev} = 506$ at $\rho = 9.5\ a_0$. This change in n_{ev} occurs because the surface functions are delocalized at smaller values of ρ and are localized at larger values of ρ which approach the asymptotic limit. Also note that $E_{cut} \approx 2\mathscr{E}_{t=100}$ provides 4 figure convergence for all the ρ values considered in Table I. This choice of E_{cut} was also found by Whitnell and Light[32] to provide good convergence for the bound states of H_3^+.

IV. RESULTS

A. Correlation diagram

The DVR surface function energies are plotted as a function of ρ in Fig. 1. These curves are the effective potentials for the ρ motion. As ρ becomes large, these energies correlate with the rovibronic states of H_2 and HF. To provide some orientation of the energy scale in Fig. 1 with respect to the reaction dynamics, asymptotic correlation energies of some H_2 and HF states are listed in Table II. For the initial state H_2 $(v = 0, j = 0)$, the relative energy $E_{rel} = E - 1.6453$ eV. In Fig. 1, a nest of curves is seen around 1.65 eV at large ρ. These correspond asymptotically to the HF $(v = 3, j = small)$ states and the H_2 $(v = 0, j = 0)$ state. If this nest of curves is followed in towards $\rho = 4$–5 a_0, other states, which correlate asymptotically with HF $(v = 2, j = large)$ states, cross through. At higher energies, another nest of curves is seen around 2.10 eV at large ρ.

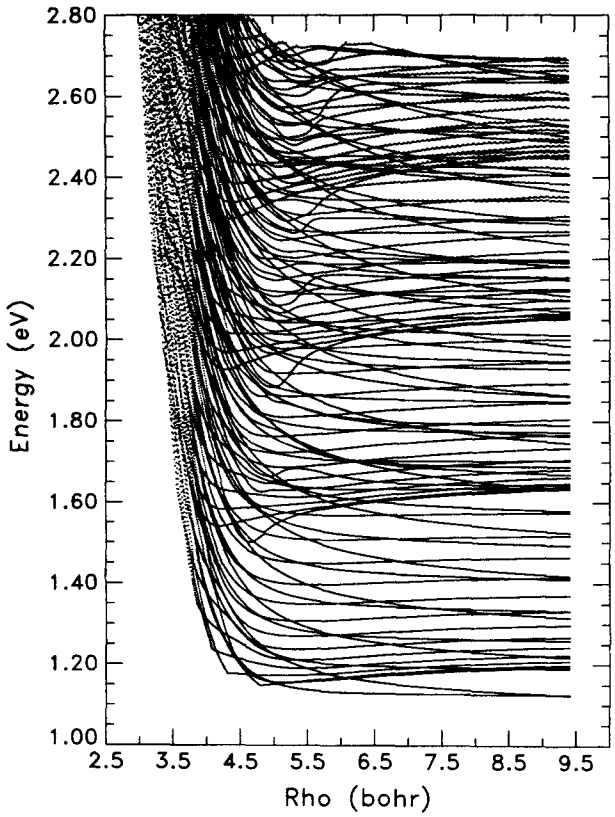

FIG. 1. Surface function eigenvalues $\mathscr{E}_t(\rho)$ [adiabatic potential curves] for $t \geqslant 30$ vs ρ (in a_0) for F + H_2 on the T5A PES. Notice that the scale for E does not start at zero.

TABLE II. Asymptotic vibrational energies $\epsilon(v, j = 0)$ for some H_2 and HF fragment states. t is the APH quantum number for the correlation at $\rho = \infty$.

Fragment	v	$\epsilon(v, j)$ (eV)	t
HF	0	0.2538	1
HF	1	0.7455	15
HF	2	1.2156	35
H_2	0	1.6453	58
HF	3	1.6642	60
HF	4	2.0914	91
H_2	1	2.1589	100
HF	5	2.4970	127

These correspond asymptotically to the HF ($v=4, j=small$) states. As these states are followed in towards small ρ, many other states cross through the $v=4$ curves. This crossing of a multitude of curves complicates the interpretation of the dynamics in terms of these adiabatic potentials.

B. Reaction probabilities

Before presenting the scattering results some nomenclature should be defined. $P^R_{v_i j_i}(v_f, j_f)$ is the distinguishable particle reaction probability from the initial H_2 rovibrational state (v_i, j_i) into *both* HF arrangement channels of final state (v_f, j_f). The reaction probability into a v_f vibrational manifold summed over all open rotational states j_f is

$$P^R_{v_i j_i}(v_f) = \sum_{j_f} P^R_{v_i j_i}(v_f, j_f). \tag{41}$$

The total reactivity, summed over all open vibrational channels v_f, is

$$P^R_{v_i j_i}(total) = \sum_{v_f} P^R_{v_i j_i}(v_f). \tag{42}$$

Quantities analagous to $P^R_{v_i j_i}(v_f, j_f)$, $P^R_{v_i j_i}(v_f)$ and $P^R_{v_i j_i}(total)$ are defined for the nonreactive probabilities as $P^{NR}_{v_i j_i}(v_f, j_f)$, $P^{NR}_{v_i j_i}(v_f)$, and $P^{NR}_{v_i j_i}(total)$, respectively, where the transition is into the final H_2 state (v_f, j_f).

For $J=0$, $P^{CH}_{v_i j_i}(v_f, j_f)$, where CH = R or NR, is calculated from the S-matrix element[20] as

$$P^{CH}_{if}(E) = \begin{cases} 2|S_{if}(E)|^2 & \text{if CH} = R \\ |S_{if}(E)|^2 & \text{if CH} = \text{NR}. \end{cases} \tag{43}$$

Here $i=(v_i, j_i)$, $f=(v_f, j_f)$, and the E dependence is explicitly specified.

In Fig. 2(a) the reaction probabilities $P^R_{00}(v_f)$ are shown as a function of total energy for F + H_2 on the T5A PES for $J=0$. A total of 95 values of E are presented where the energy resolution is provided in Table III. These curves show much structure. The $P^R_{00}(2)$ is far from smooth with local maxima near 1.66, 1.83, 2.04, and 2.09 eV. $P^R_{00}(3)$ and $P^R_{00}(total)$ exhibit both dips and peaks. Also note the extremely sharp threshold behavior of $P^R_{00}(4)$ near 2.10 eV. $P^R_{00}(4)$ increases from zero to nearly 0.15 over an interval of less than 0.01 eV. $P^R_{00}(2)$ and $P^R_{00}(3)$ are replotted in Fig. 2(b) along with the results of Yu *et al.*[16] calculated for $E=[1.671, 1.797]$ eV using a variational method. The present results agree quite well with those of Yu *et al.* This agreement, coupled with the fact that two independent scattering methods were used (our propagation vs their variational), leads us to conclude that both calculations are converged and accurate.

In Figs. 3(a) and 3(b) the state-to-state reaction probabilities $P^R_{00}(v_f, j_f)$ for $v_f=2$ are shown as a function of total energy and of final rotational state j_f. Figure 3(b) is a continuation of Fig. 3(a) in E space. The distribution in Fig. 3 is fairly sharp in many regions of E and j_f space. The most probable j_f value, max(j_f), for $P^R_{00}(2, j_f)$ shifts as a function of energy. At 1.73 eV, max(j_f) = 6; at 1.86 eV, max(j_f) = 11; and, at 2.04 eV, max(j_f) = 13. Also, more than one local maximum in $P^R_{00}(2, j_f)$ can be observed for many fixed values of E. A second peak, with respect to the max(j_f) peaks discussed above, occurs centered about 1.90 eV and $j_f=3$. At energies above 2.10 eV three and four distinct peaks can be discerned. At the highest energy plot-

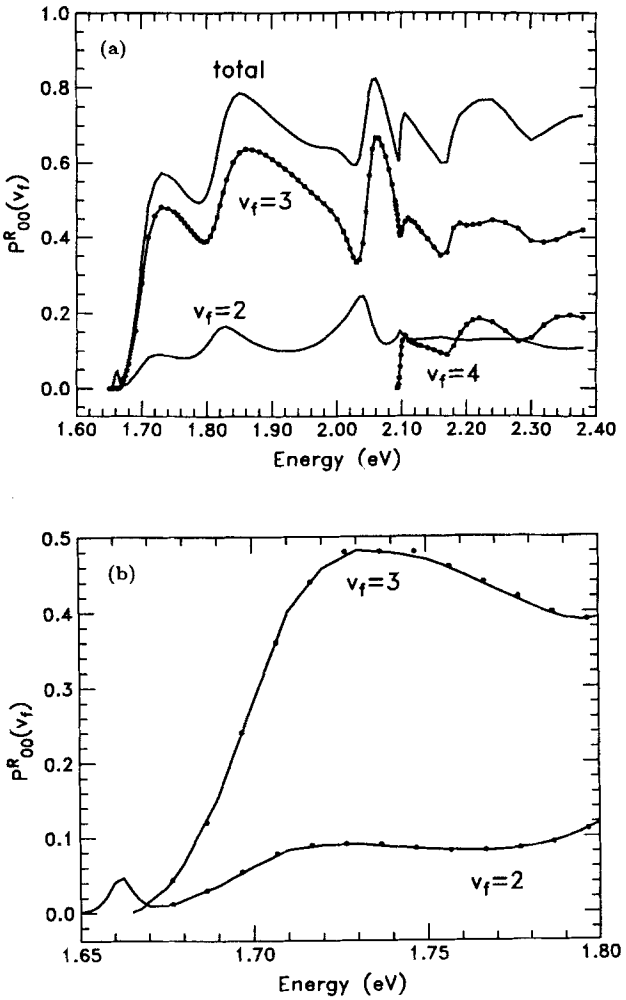

FIG. 2. (a) F + H_2 reaction probabilities $P^R_{00}(v_f)$ for $J=0$ plotted vs total energy. Legend: (lower solid line) $v_f=2$; (upper connected dots) $v_f=3$; (lower connected dots) $v_f=4$; (upper solid line) total reactivity. The dots, which are connected for clarity, are the actual calculations. The energy resolution is provided in Table III. Between 1.645 and 1.665 eV, $P^R_{00}(2)$ and $P^R_{00}(total)$ are identical. $E_{rel} = E - 1.6453$ eV. (b) F + H_2 reaction probabilities $P^R_{00}(2)$ and $P^R_{00}(3)$ for $J=0$ plotted vs total energy. The lower and upper solid lines are the present results for $v_f=2$ and $v_f=3$, respectively. The dots are the results of Yu *et al.* (Ref. 16). Note the change in scale of both axes with respect to Fig. 2(a).

TABLE III. The resolution of the total scattering energies E on various intervals for the calculations presented.

Resolution (eV)	Interval(s) (eV)
0.001	[2.09,2.10]
0.0025	[1.65,1.68]
0.005	[1.75,1.83]; [2.01,2.09]; [2.10,2.13]
0.01	[1.68,1.75]; [1.83,2.01]; [2.13,2.22]
0.02	[2.22,2.40]

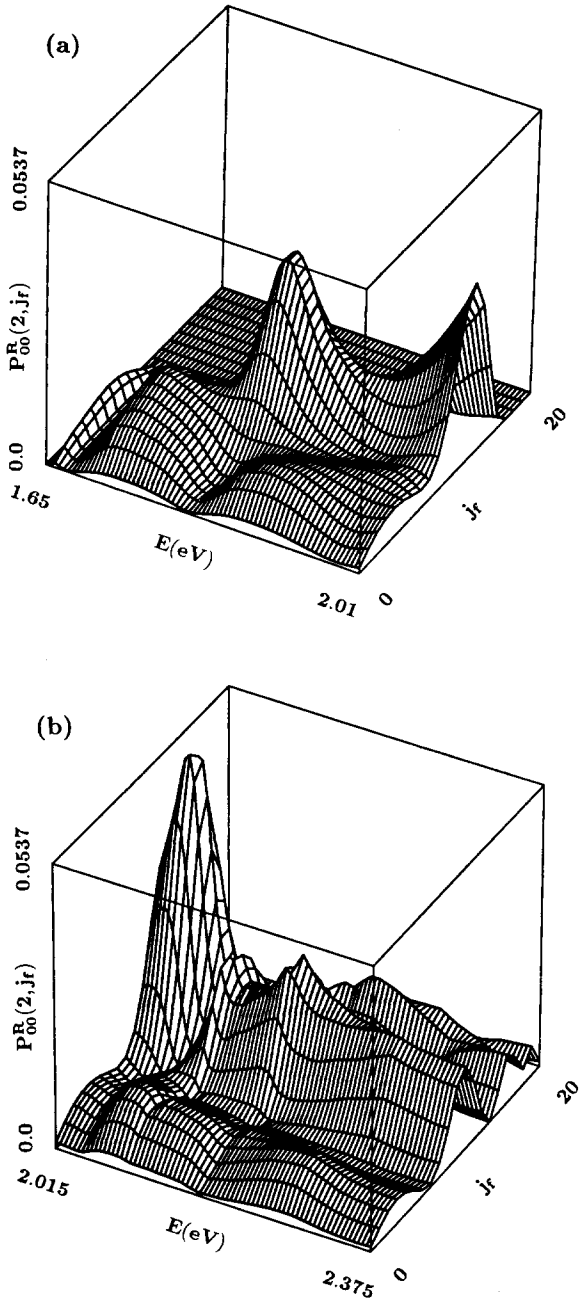

FIG. 3. (a) $P^R_{00}(v_f, j_f)$ for $v_f = 2$ plotted vs total energy E along the x axis and j_f along the y axis. E runs from 1.65 ($\approx$ total reaction threshold) to 2.01 eV in increments of 0.005 eV. (b) Same as (a), except that E runs from 2.015 to 2.375 eV.

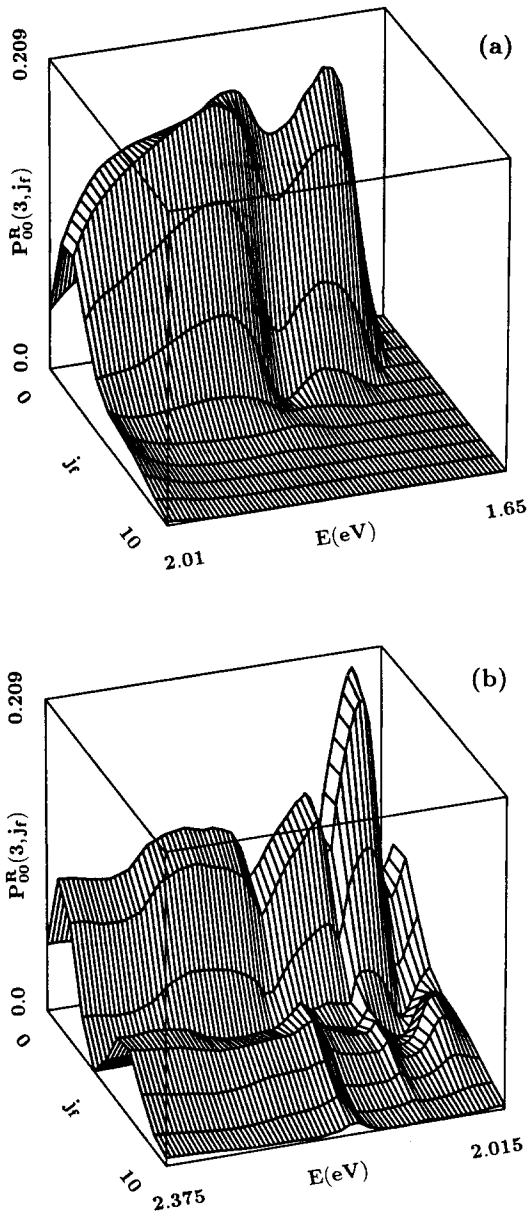

FIG. 4. (a) $P^R_{00}(v_f, j_f)$ for $v_f = 3$ plotted vs j_f along the x axis and total energy E (right to left) along the y axis. E runs from 1.65 ($\approx$ total reaction threshold) to 2.01 eV in increments of 0.005 eV. (b) Same as (a), except that E runs from 2.015 to 2.375 eV.

ted, 2.375 eV, four peaks are seen centered at $j_f = 3$, 11, 16, and 19.

Figures 4(a) and 4(b) are the same as Figs. 3, except that $v_f = 3$. Up to energies of 2.01 eV, the $P^R_{00}(3, j_f)$ consist of a single peak in j_f space for fixed values of E. Centered about $E = 2.10$ and 2.18 eV, a decrease in $P^R_{00}(3, j_f = 1,2)$ is accompanied by a concurrent increase in $P^R_{00}(3, j_f = 6,7)$. That is, the shoulders in $P^R_{00}(3, j_f)$ at large j_f line up with the dips in $P^R_{00}(3, j_f)$ at small j_f. At the highest energy plotted, 2.375 eV, the j_f distribution is also bimodal with peaks centered at $j_f = 1$ and 6. The probabilities presented in Figs. 3 and 4 were generated for each value of j_f by a linear interpolation of the probabilities calculated at the E values listed in Table III.

In Fig. 5 the nonreactive probabilities $P^{NR}_{00}(0, j_f)$ are plotted for $j_f = 0$ (elastic) and $j_f = 2$, 4, and 6 inelastic. These curves also show much structure. For example, it is difficult to follow the curves around 2.00–2.10 eV as $P^{NR}_{00}(0,0)$ and $P^{NR}_{00}(0,2)$ plunge to nearly zero while at the same time $P^{NR}_{00}(0,4)$ achieves a local maximum.

The reaction probabilities out of excited initial states, $P^R_{02}(v_f)$, $P^R_{04}(v_f)$, and $P^R_{10}(v_f)$, are shown in Figs. 6, 7, and 8, respectively. At threshold near 2.10 eV, $P^R_{02}(4)$ and $P^R_{04}(4)$ increase quite sharply as was the case for $P^R_{00}(4)$ in

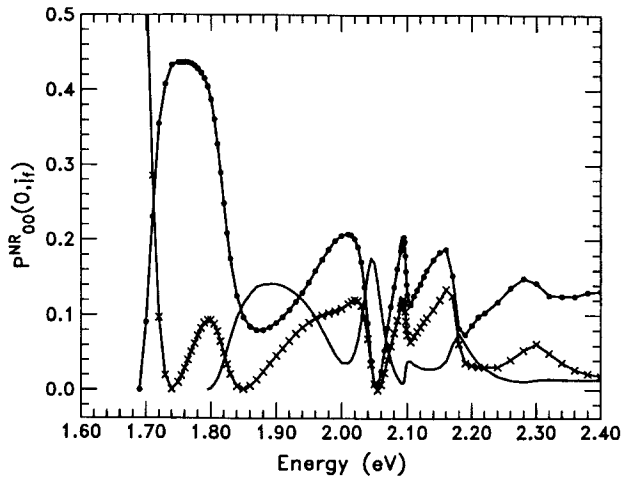

FIG. 5. F + H_2 nonreactive probabilities $P^{NR}_{00}(0, j_f)$ for $J = 0$ plotted vs total energy E. Legend: ($\times$ line) $j_f = 0$ [elastic]; (connected dots) $j_f = 2$; (solid line) $j_f = 4$. Note the scale of the probability axis; $P^{NR}_{00}(0,0) > 0.5$ for E between threshold and 1.70 eV.

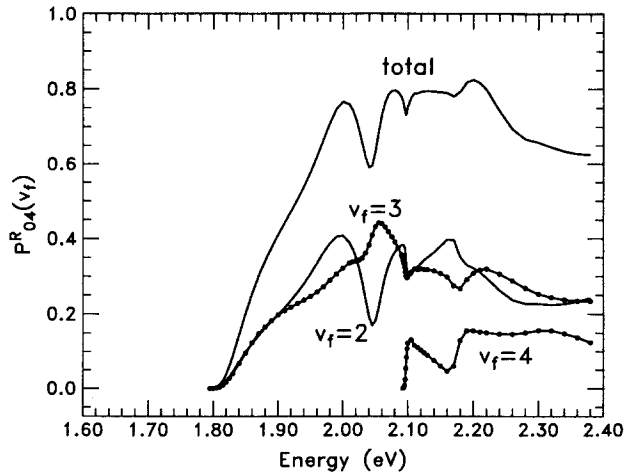

FIG. 7. Same as Fig. 6, except that $P^R_{04}(v_f)$ is plotted. $E_{rel} = E - 1.7909$ eV.

Fig. 2(a). The P^R_{02} in Fig. 6 are qualitatively similar in some respects to those in Fig. 2(a); however, for $E = [1.70,2.00]$ eV, the ratio of $P^R_{02}(2)$:$P^R_{02}(3)$ is somewhat larger than the ratio of $P^R_{00}(2)$:$P^R_{00}(3)$. Also, near 1.83 eV the peak in $P^R_{02}(2)$ is more pronounced than the peak in $P^R_{00}(2)$. For the feature near 2.06 eV, $P^R_{02}(3)$ and $P^R_{02}(total)$ look like the P^R_{00} counterparts, while the peak in $P^R_{02}(2)$ is shifted to higher energy with respect to the peak in $P^R_{00}(2)$.

In Fig. 7, the ratio of $P^R_{04}(2)$:$P^R_{04}(3)$ is nearly 1:1 over the range $E = [1.80,1.90]$ eV. The feature near 2.06 eV appears different from that in Figs. 2 and 6. There is now a significant dip in $P^R_{04}(2)$ centered near 2.06 eV, and the peak in $P^R_{04}(3)$ is barely discernible above the monotonically increasing portion of the curve before it.

The probabilities plotted in Fig. 8 are not as well converged with respect to the number of adiabatic surface functions as in Figs. 2, 6, and 7. Still, these preliminary results show that HF $v_f = 4$ is by far the predominant final channel for $J = 0$ scattering out of H_2 ($v_i = 1, j_i = 0$). This propensity for $v_f = 4$ is in direct contrast with the other probabilities examined thus far for scattering out of H_2 ($v_i = 0, j_i$) states.

C. Convergence studies

In our earlier paper,[17] a convergence study for $P^R_{00}(v_f)$ was presented as a function of the number of adiabatic surface functions N. For $N = 150$, $P^R_{00}(total)$, $P^R_{00}(4)$, $P^R_{00}(3)$, and $P^R_{00}(2)$ appear to be converged to within 2% for $E = [1.70,2.40]$ eV except near $E = 2.10$ eV where the convergence is not quite as good. This sensitivity near $E = 2.10$ eV is due to a closed-channel resonance which will be examined later. Also, for $N = 150$, the S matrices are unitary to a part per thousand or better even at $E = 2.40$ eV. $N = 150$ was used for all the calculations reported in this work.

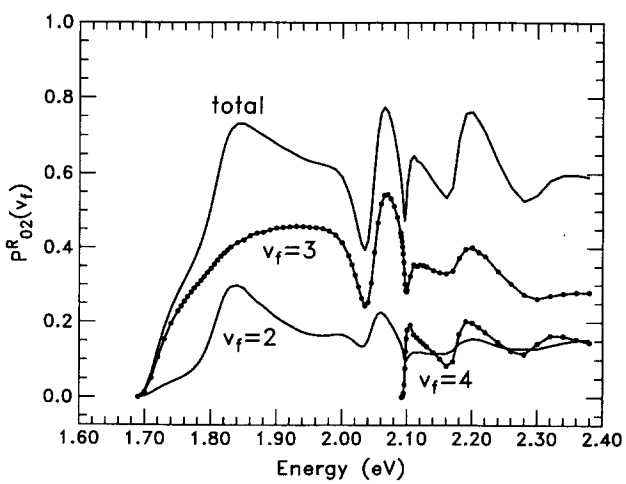

FIG. 6. F + H_2 reaction probabilities $P^R_{02}(v_f)$ for $J = 0$ plotted vs total energy E. Legend: (lower solid line) $v_f = 2$; (upper connected dots) $v_f = 3$; (lower connected dots) $v_f = 4$; (upper solid line) total reactivity. $E_{rel} = E - 1.6894$ eV.

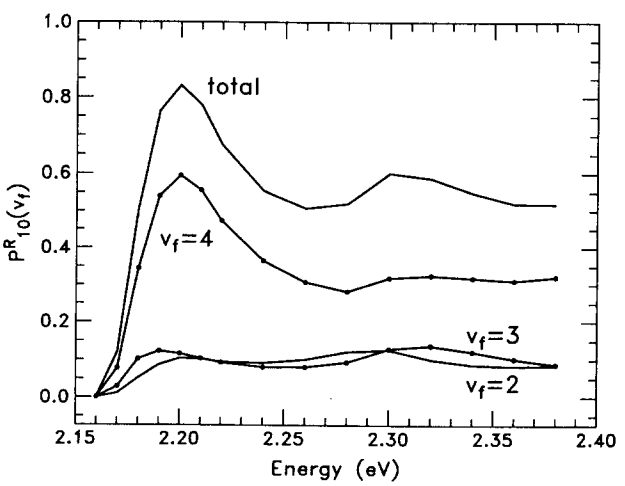

FIG. 8. Same as Fig. 6, except that $P^R_{10}(v_f)$ is plotted. Legend: (lower solid line) $v_f = 2$; (lower connected dots) $v_f = 3$; (upper connected dots) $v_f = 4$; (upper solid line) total reactivity. Note the scale of the energy axis. $E_{rel} = E - 2.1589$ eV.

The spacing between successive ρ_ξ values was governed by Δ_ξ where

$$\rho_{\xi+1} = (1 + \Delta_\xi)\rho_\xi. \tag{44}$$

$\Delta_\xi = 0.01$ was used here. If Δ_ξ is too large, the expansion of the surface functions at the outer boundary of the ξ th sector in terms of the surface functions calculated in the $(\xi + 1)$th sector becomes incomplete. This in turn degrades the propagated solution to the CC equations. Although convergence with respect to Δ_ξ was not investigated for $F + H_2$, $\Delta_\xi = 0.01$ did provide accurate reaction probabilities for $J = 0$ calculations[36] on $H + H_2$.

The number of log-derivative steps taken within a given sector, $n_{\text{steps}}(\xi)$, is based upon the de Broglie wavelength

$$\lambda = \frac{2\pi}{[2\mu E]^{1/2}}, \tag{45}$$

where E is the largest scattering (total) energy (in atomic units) for a given scattering production run. For each sector of length $\delta\rho_\xi = \rho_{\xi+1} - \rho_\xi = \Delta_\xi\rho_\xi$, $n_{\text{steps}}(\xi)$ is given as

$$n_{\text{steps}}(\xi) = \text{INT}\left[n_\lambda \times \left(\frac{\delta\rho_\xi}{\lambda} \right) + 0.9 \right], \tag{46}$$

where INT denotes integer truncation of the argument and $n_\lambda \approx$ number of steps per λ. In order to verify convergence with respect to n_λ, reaction probabilities at 2.10 and 2.40 eV were calculated using the appropriate value of λ for 2.40 eV, $\lambda = 0.359\ a_0$. For $n_\lambda = 20$ vs 30, reaction probabilities at 2.10 and 2.40 eV were calculated, and the values of $P_{00}^{\text{NR}}(v)$ for $v = 0$ and 1 and $P_{00}^{R}(v)$ for $v = 0$–4 were compared. Both the 2.10 and 2.40 eV results were identical to three figures. Hence, the apparently converged value of $n_\lambda = 20$ was used in the rest of our calculations.

The asymptotic correlation of the basis is as follows. For transitions out of H_2 initial states with *even* j only surface functions which correlate with *even* j are needed in the H_2 arrangement channel whereas correlation with *all* j is needed in the HF arrangements. The notation $(j_0, j_1, \ldots, j_v)$ denotes the highest j state included within the v vibrational manifold. For $N = 150$, the correlations are H_2 channel = (12,8,2) and HF channels (31,28,24,21,16,10). We also note that our *adiabatically determined* basis is better than a strictly asymptotic basis containing the same number of functions.

D. The *S* matrix and related quantities

An S matrix element can be expressed as

$$S_{if}(E) = r_{if}(E)\exp[i\phi_{if}(E)], \tag{47}$$

where r_{if} is the magnitude and ϕ_{if} is the phase. The phase obtained by decomposing a calculated $S_{if}(E)$ using Eq. (47) can only be determined to modulo 2π. In order to obtain a single-valued function of E for $\phi_{if}(E)$ from the calculated $S_{if}(E)$ values, a program was implemented[37] which determines ϕ_{if} in a relative sense by adding or subtracting multiples of 2π to the calculated $\phi_{if}(E)$. After the relative phase is assigned, a cubic spline fit to both $\ln[r_{if}(E)]$ and $\phi_{if}(E)$ is performed for each specified transition pair *if*. The results of this procedure for the transitions $i = H_2$ $(v_i = 0, j_i = 0)$ and $f = HF$ $(v_f = 3, j_j = 0$–$3)$ are presented in Fig. 9. Each curve is shifted downwards by 4π radian for each subsequent *if* value for clarity in presentation. The behavior of these four curves is qualitatively similar: $\phi_{if}(E)$ is a monotonically decreasing function of E. Thus, $d\phi/dE$ is negative for all values of E. In fact, this qualitative behavior is true for *all* of the $\phi_{if}(E)$ we have examined where $i = H_2$ $(v_i = 0, j_i = 0)$. The steepness of the phase, especially at the lower energies, reflects the repulsive nature of the interaction potential for $F + H_2$. There are a couple of inflection points in the curves in Fig. 9 which are suggestive of some interesting properties which we will discuss later in a different context.

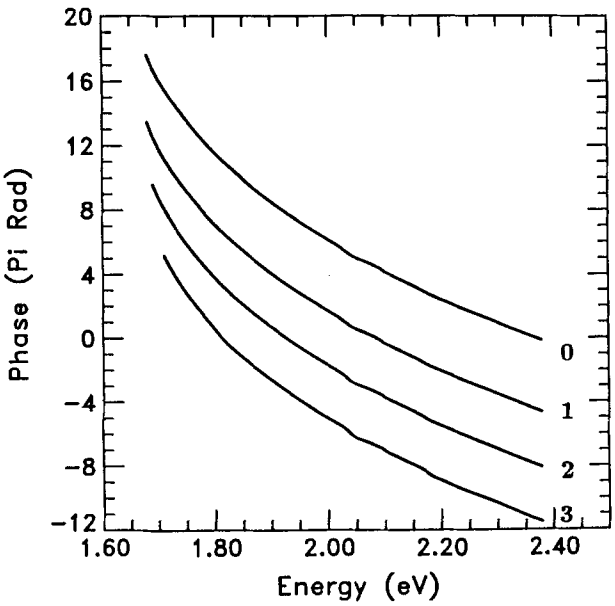

FIG. 9. The phase $\phi_{if}(E)$, for transitions $i = H_2$ $(v_i = 0, j_i = 0)$ to $f = HF$ $(v_f = 3, j_f)$ for $j_f = 0$–3, plotted as a function of energy. For clarity in presentation, each successive curve is offset by 4π radians.

In Fig. 10 Argand diagrams are presented for the S matrix elements $i = H_2(v_i = 0, j_i = 0)$ and $f = HF(v_f = 2, j_f = 4$–$7)$. An Argand diagram is a polar plot of $S_{if}(E)$ along the trajectory in E space, where $r_{if}(E)$ is the radial coordinate and $\phi_{if}(E)$ is the polar angle. The diagrams in Fig. 10 are plotted along the energy trajectory $E = [1.65, 1.70]$ eV. Each point represents a calculated value and the continuous line connecting the points is obtained from the cubic spline fit to Eq. (47). Figure 11 is the same as Fig. 10, except that $f = HF$ $(v_f = 2, j_f = 9$–$12)$ and the trajectory is $E = [1.83, 2.115]$ eV. Figure 12 is the same as Fig. 10, except that $f = HF$ $(v_f = 2, j_f = 0$–$3)$ and the trajectory is $E = [1.91, 2.115]$ eV.

In Fig. 13 Argand diagrams are shown for two nonreactive transitions where $i = H_2(v_i = 0,\ j_i = 0)$ and $f = H_2(v_f = 0, j_f = 0)$; elastic, and $f = H_2$ $(v_f = 0, j_i = 2)$; inelastic. The trajectory is $E = [1.95, 2.13]$ eV. The energy resolution of the points in Figs. 10–13 is summarized in Table III.

We next consider two quantities introduced by Smith[38] for analyzing long-lived states and resonances: the state-to-state time delay and the collision lifetime matrix. Both are constructed from the S matrix and its energy derivative. The state-to-state time delay is

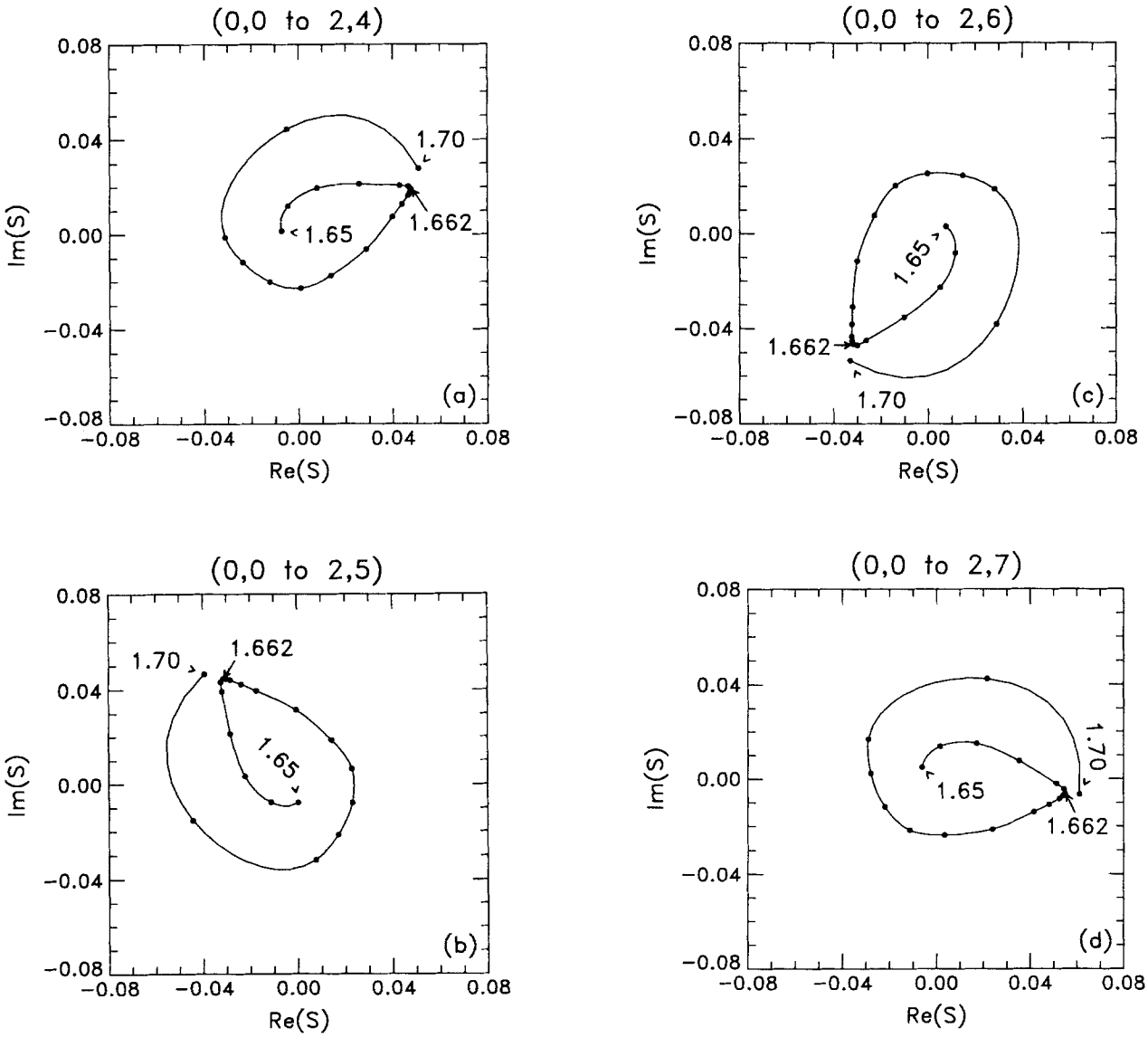

FIG. 10. Argand diagrams for the reactive transitions $i = H_2$ ($v_i = 0, j_i = 0$) to $f =$ HF ($v_f = 2, j_f$) along the trajectory $E = [1.65, 1.70]$ eV. Each dot represents a calculated value, where the energy resolution is provided in Table III augmented by 4 more calculations at 1.661, 1.662, 1.663, and 1.664 eV. (a) $j_f = 4$. (b) $j_f = 5$. (c) $j_f = 6$. (d) $j_f = 7$.

$$\Delta t_{if} = \mathrm{Real}\left\{ -i\hbar [S_{if}(E)]^{-1}\left(\frac{dS_{if}(E)}{dE}\right)\right\} . \tag{48}$$

A physical interpretation of Δt_{if} is the time for observing a wave packet which has transversed the interaction potential relative to the time of observing the same wave packet which has transversed a zero potential.

The collision lifetime matrix is

$$\mathbf{Q} = i\hbar \mathbf{S}\left(\frac{d\mathbf{S}}{dE}\right)^{\dagger} . \tag{49}$$

Upon diagonalization of **Q**, the eigenvalues (eigenlifetimes $= \tau$) and eigenvectors contain information about resonances. In particular, a positive value of τ implies a long-lived state and the eigenvector for τ yields the asymptotic states which are participating in the resonance.[39] Δt_{if} is much easier to construct than **Q** for a given E, since for Δt_{if} only a *single* element of $S_{if}(E)$ and its derivative is needed, whereas for **Q** the *whole* **S** matrix and its derivative is needed. This difference has some bearing on the accuracy of Δt_{if} vs **Q** since $d\mathbf{S}/dE$ is obtained by differentiating the cubic spline fit to Eq. (47). $d\mathbf{S}/dE$ will only be as accurate as the fit. For a single transition it is easy to monitor the quality of the fit. But to construct, for example, a 100×100 **Q** matrix we need $(100 \times 101)/2$ elements of $d\mathbf{S}/dE$ (**Q** is Hermitian.) It is then assumed that all $\approx 10\,000$ cubic spline fits are accurate for all transitions i to f. One way around this problem is to compute $d\mathbf{S}/dE$ directly during the propagation of the scattering wave function. This would eliminate the uncertainty in $d\mathbf{S}/dE$ due to the fitting procedure. Research along this line has been demonstrated by Hayes and

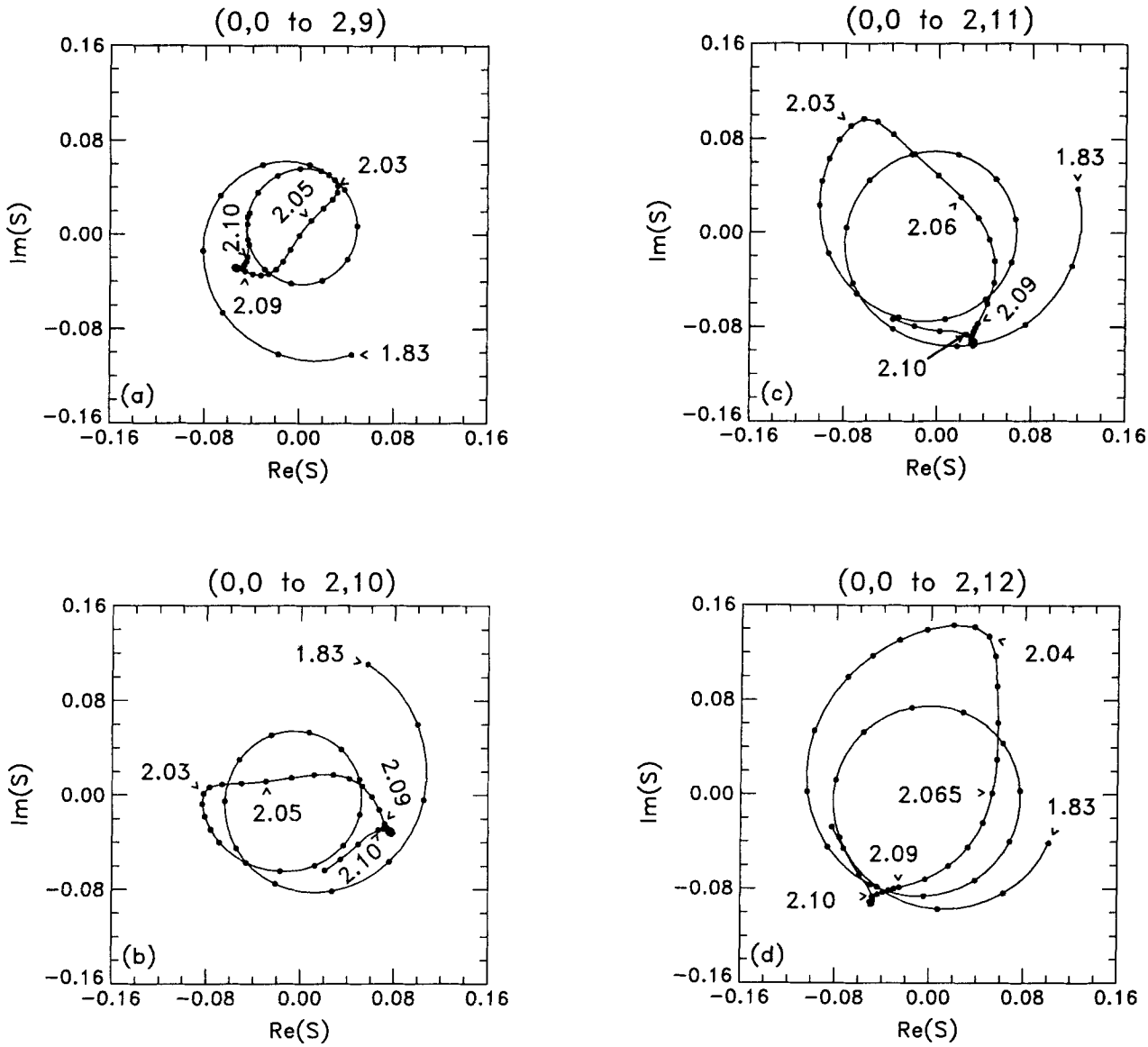

FIG. 11. Same as Fig. 10, except the trajectory $E = [1.83, 2.115]$ eV. The energy resolution is provided by Table III (unaugmented). (a) $j_f = 9$. (b) $j_f = 10$. (c) $j_f = 11$. (*d*) $j_f = 12$.

Walker,[40] and we hope to implement their approach in the future.

In Fig. 14(a) state-to-state time delays Δt_{if} are presented for the transitions from $i = H_2(v_i = 0,\ j_i = 0)$ to $f = HF(v_f = 3, j_f)$ for $j_f = 0$–3. Time delays for the same transitions were presented by Yu *et al.*[16] over the range $E = [1.676, 1.827]$ eV which agree quite well with the curves in Fig. 14(a). Figure 14(b) is the same as Fig. 14(a) except that $f = HF\ (v_f = 2, j_f)$ for $j_f = 13$, 12, 11, and 10. Figure 15 is the same as Figure 14(a), except that $i = H_2(v_i = 0, j_i = 0)$ to $f = HF\ (v_f = 2, j_f)$ for $j_f = 6$–9.

Eigenlifetimes of the **Q** matrix are presented in Tables IV, V, and VI. In Table IV, the eigenlifetime is listed whose eigenvector is predominantly a nearly equal mixture of HF states $(v = 2, j)$ for $j = 2$–9 in the range $E = [1.655, 1.665]$ eV. In Table V, the eigenlifetime is listed whose eigenvector is predominantly a nearly equal mixture of H_2 states $(v = 0, j)$ for $j = 0$, 2, and 4 and of HF states $(v = 3, j)$ for $j = 1$, 2, and 3 in the range $E = [2.03, 2.065]$ eV. Finally, in Table VI, the eigenlifetime is given whose eigenvector is predominantly a nearly equal mixture of H_2 states $(v = 0, j)$ for $j = 0$,2 and 4 and of HF states $(v = 3, j)$ for $j = 1$–6 in the range $E = [2.093, 2.098]$ eV.

V. DISCUSSION

A. Reaction probabilities, Argand diagrams, time delays, and collision lifetimes

To provide some continuity in presentation, this section will be arranged by discussing the results, presented in the last section, in order of total energy starting from the reaction threshold of 1.6453 eV.

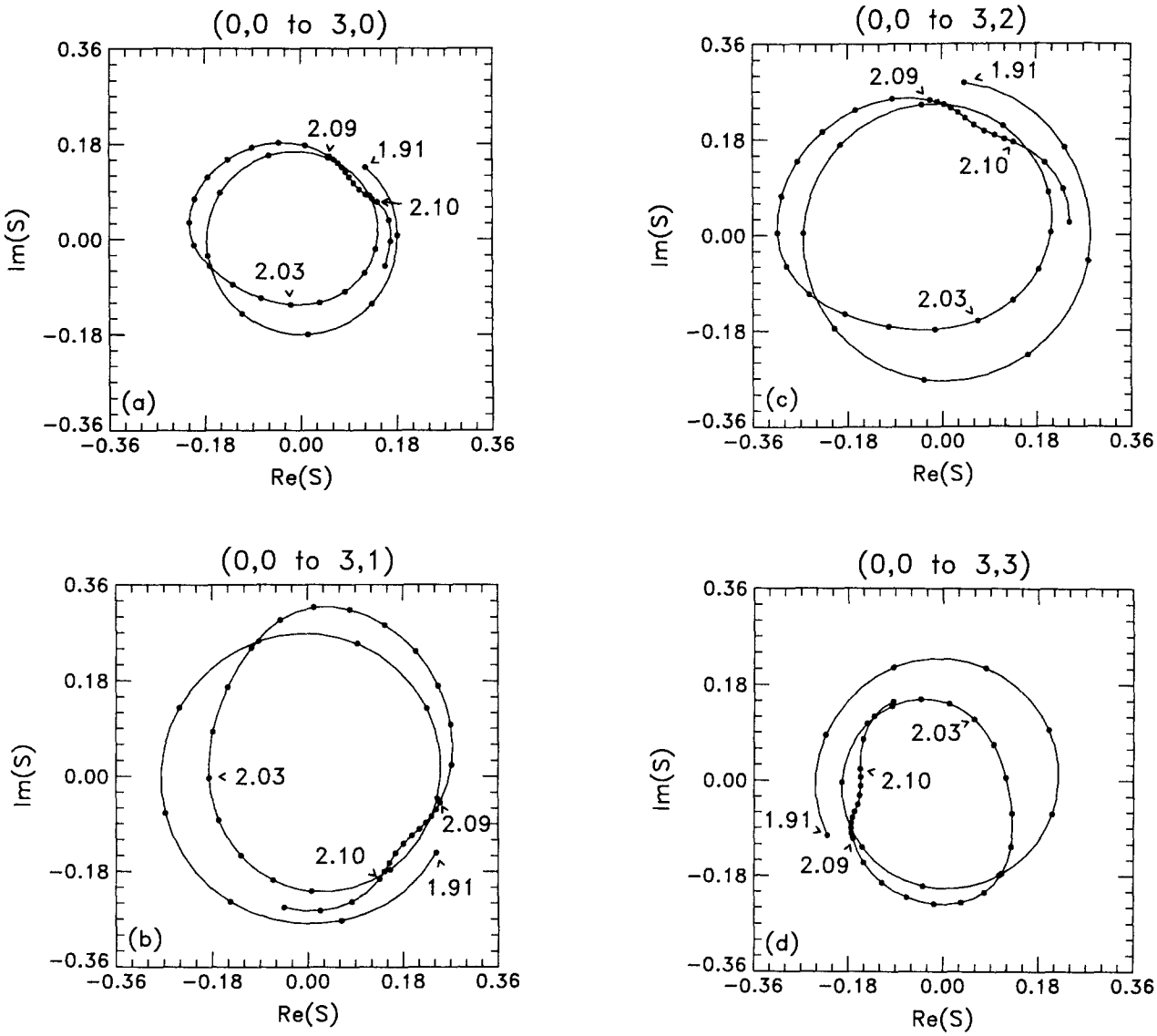

FIG. 12. Same as Fig. 10, except $v_f = 3$ and the trajectory $E = [1.91, 2.115]$ eV. The energy resolution is provided by Table III (unaugmented). (a) $j_f = 0$. (b) $j_f = 1$. (c) $j_f = 2$. (d) $j_f = 3$.

1. 1.645–1.67 eV

A bit past the reaction threshold a small peak is observed in $P^R_{00}(2)$ at 1.6625 eV in Fig. 2(a). This small peak in the probability is due to a closed channel resonance as the HF ($v = 3$) states do not begin to open until 1.6642 eV. The distribution of final rotational states within this peak is illustrated in the plot of $P^R_{00}(2, j_f)$ in Fig. 3(a), where at 1.6625 eV a sharp feature in energy space is seen with a most probable j_f value, $\max(j_f)$, equal to 6. This resonance is also evident in the time delays presented in Fig. 15. Contrast the curves in Fig. 15 with those in Fig. 14(a) in the threshold energy region 1.65 to 1.75 eV. The curves in Fig. 14(a) in the threshold region are typical for nonresonant transitions we have examined: the time delay is monotonically increasing from an initially very negative value. The curves in Fig. 15 in the threshold region appear to have a sharp spike centered about 1.6625 eV superimposed onto a nonresonant monotonically increasing background. This spike is a signature that these transitions, $i = H_2$ ($v_i = 0$, $j_i = 0$) to $f =$ HF ($v_f = 2$, $j_f = 2$–9), are participating in the resonance.

This resonance in the threshold region also appears in the Argand diagrams shown in Fig. 10. The typical energy trajectory for an S-matrix element of a nonresonant background is that of a smoothly swirling path rotating in a clockwise direction ($d\phi/dE$ is negative). As a trajectory is followed in Fig. 10, it begins to swirl smoothly until it encounters a kink at 1.6625 eV. After this kink, the trajectory then begins to swirl smoothly again. This kink results from $d\phi/dE$ becoming less negative at 1.6625 eV. Although $d\phi/dE$ is *not* positive in an absolute sense, it is more positive with respect to the "background" $d\phi/dE$. For an isolated single channel resonance ϕ increases by 2π as it passes through the

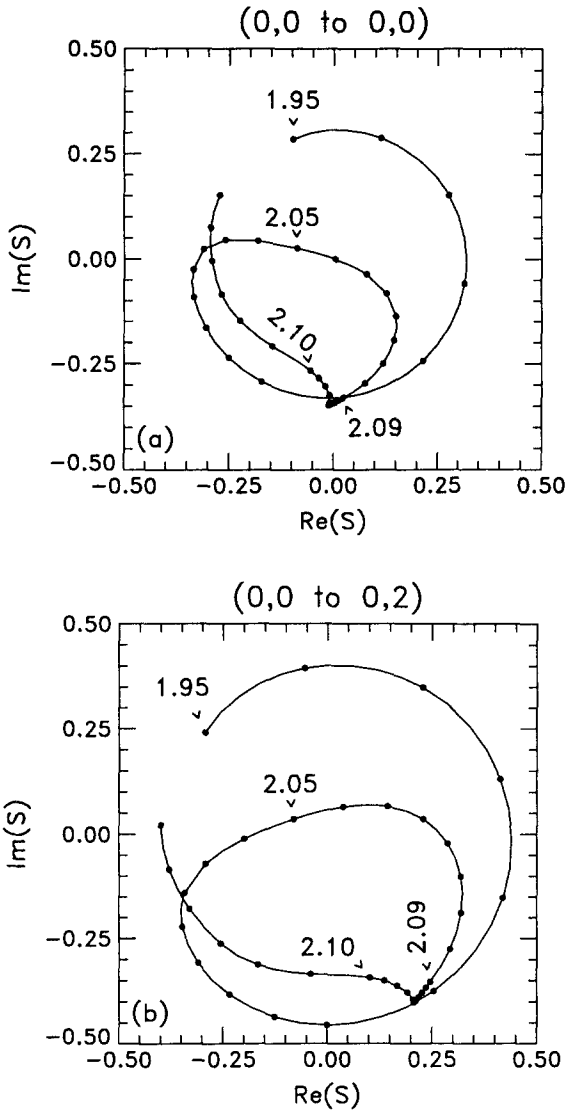

FIG. 13. Argand diagrams for the nonreactive transitions $i = H_2$ ($v_i = 0, j_i = 0$) to $f = H_2$ ($v_f = 0, j_f$) along the trajectory $E = [1.95, 2.13]$ eV. Each dot represents a calcualted value, where the energy resolution is provided in Table III. (a) $j_f = 0$, elastic. (b) $j_f = 2$, inelastic.

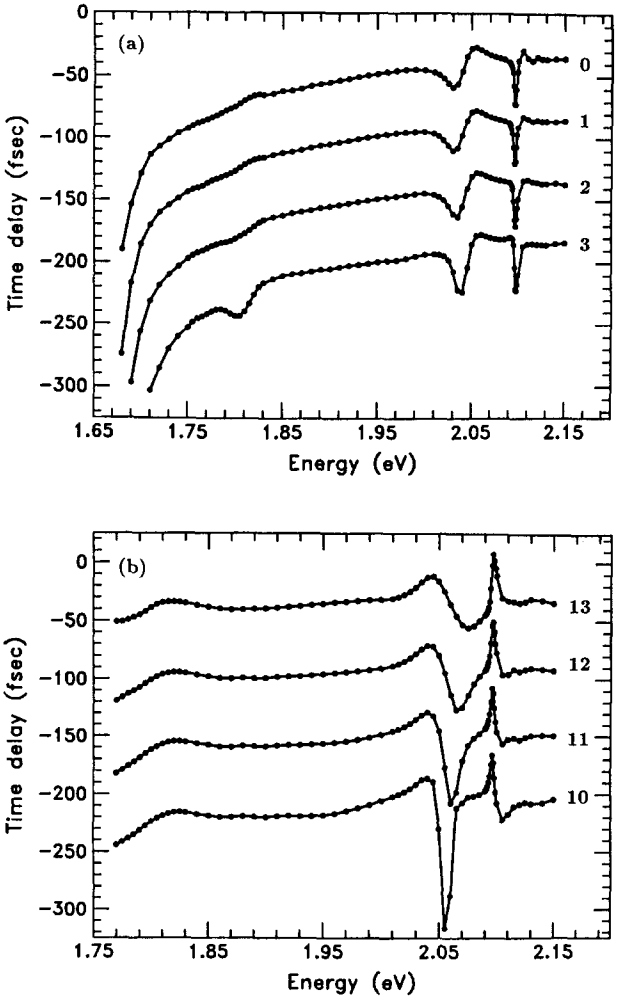

FIG. 14. (a) Time delays for the reactive transitions $i = H_2$ ($v_i = 0, j_i = 0$) to $f = HF$ ($v_f = 3, j_f$) for $j_f = 0$–3. For clarity in presentation, each successive curve is offset by -50 fs. (b) Same as (a), except $v_f = 2$ and $j_f = 13$, 12, 11, and 10, and each successive curve is offset by -60 fs.

resonance; $d\phi/dE$ is positive. Therefore, the kink in the Argand diagram indicates that these transitions are participating in a multichannel resonance as each $d\phi/dE$ becomes much less negative at 1.6625 eV.

The final piece of information about the resonance at threshold comes from the analysis of the eigenlifetimes of the collision lifetime matrix in Table IV. These data indicate the existence of a resonance near 1.66 eV with a lifetime $\tau \approx 230$ femtoseconds (fs) which involves the HF states ($v = 2$, $j = 2$–9). The accuracy of the lifetime estimate is probably good to $\pm$ 10% due to the uncertainty in the numerical fitting procedure, discussed earlier, used to determine $d\,\mathrm{S}/dE$.

2. 1.67–1.90 eV

The next energy region of interest is between 1.67 and 1.90 eV. In Fig. 2(a), $P_{00}^{R}(3)$ peaks near 1.73 eV, dips near

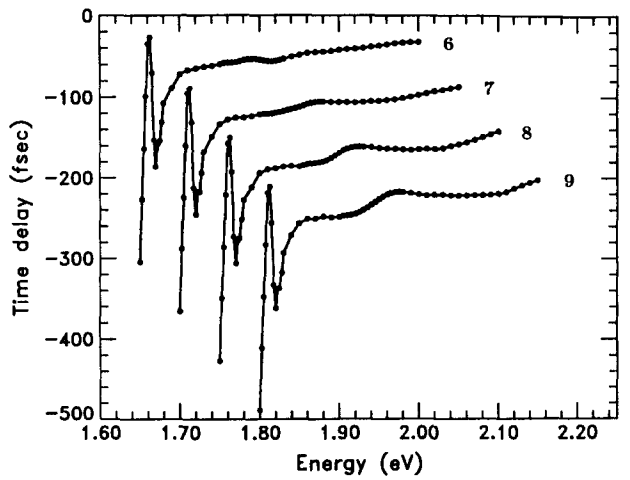

FIG. 15. Same as Fig. 14(a), except $v_f = 2$ and $j_f = 6$–9. For clarity in presentation, each successive curve is offset by -50 fs *and* by $+0.05$ eV.

TABLE IV. The eigenvalue (eigenlifetime) τ in femtoseconds (fs) of the collision lifetime matrix whose eigenvector is predominantly a nearly equal mixture of HF states ($v = 2$, j) for $j = 2$–9.

	E (eV)				
	1.655	1.6575	1.66	1.6625	1.665
τ (fs)	80	160	230	220	97

1.80 eV and peaks again at 1.86 eV. Meanwhile, $P_{00}^{R}(2)$ shows a broad local maximum around 1.72 eV, a broad dip about 1.77 eV and a definite peak at 1.83 eV. This behavior suggests that the HF $v = 2$ and 3 states are participating in some sort of broad resonance and/or quantum effect. Perhaps the most dramatic feature in the analysis of the reaction probabilities over this energy range is the shift of the most probable j_f value, max(j_f), in Figs. 3(a) and 3(b) for $P_{00}^{R}(2, j_f)$ as a function of energy. This shift in max(j_f) with respect to energy suggests a highly quantized rotational motion for this system. Other evidence for a broad resonance in this energy region is apparent in the time delays plotted in Figs. 14(a), 14(b), and 15. In Fig. 14(a), there is a subtle inflection point in the curves about 1.81 eV. In Fig. 14(b), the curves quit increasing monotonically at about 1.81–1.82 eV and exhibit a slight hint of a broad maximum before continuing at a plateau value on up to 1.90 eV. The curves in Fig. 15 also show an inflection point around 1.80 eV.

A very interesting phenomenon is observed in the plot of $P_{00}^{NR}(0, j_f)$ in Fig. 5. The inelastic transition $P_{00}^{NR}(0,2)$ peaks quite strongly centered at about 1.76 eV. It seems that the transfer of reaction flux from HF ($v = 3$) states [see Fig. 2(a)] back into the H_2 ($v = 0$, j = 2) state is very efficient over the energies of 1.70 to 1.83 eV. Also, after the elastic transition $P_{00}^{NR}(0,0)$ falls to nearly zero at 1.74 eV, it then shows a small peak centered at about 1.79 eV. Thus, the H_2 ($v = 0$, j = 0) state is also involved in this process to a lesser extent. Notice also that the H_2 ($v = 0, j = 4$) threshold is at 1.791 eV. The opening of this channel may also play a role in causing some of the features seen in $P_{00}^{R}(2)$ in Fig. 2(a).

In summary, the quantum effect/broad resonance that causes the dip in the reaction probability near 1.80 eV is probably due to a nonreactive resonance involving the H_2 ($v = 0, j = 2$) state, and the decrease in reactivity is simply due to conservation of flux. This conclusion is further amplified in later discussions of the 1D and reduced 3D results.

3. 1.90–2.00 eV

Between 1.90 and 2.00 eV nothing significant occurs in terms of the features observed in Fig. 2(a). $P_{00}^{R}(total)$ and $P_{00}^{R}(3)$ are monotonically decreasing and $P_{00}^{R}(2)$ is monotonically increasing as function of energy.

TABLE V. The eigenvalue (eigenlifetime) τ in femtoseconds (fs) of the collision lifetime matrix whose eigenvector is predominantly a nearly equal mixture of H_2 states ($v = 2$, j) for $j = 0,2$, and 4, and of HF states ($v = 3$, j) for $j = 1,2$, and 3.

	E (eV)							
	2.03	2.035	2.04	2.045	2.05	2.055	2.06	2.065
τ (fs)	4	18	28	36	35	22	18	2

TABLE VI. The eigenvalue (eigenlifetime) τ in femtoseconds (fs) of the collision lifetime matrix whose eigenvector is predominantly a nearly equal mixture of H_2 states ($v = 2$, j) for $j = 0,2$, and 4, and of HF states ($v = 3$, j) for $j = 1$–6. HF ($v = 4$, j = 0) is in the mixture at 2.096, 2.097, and 2.098 eV. HF ($v = 4$, j = 1) is in the mixture at 2.099 eV.

	E (eV)						
	2.093	2.094	2.095	2.096	2.097	2.098	2.099
τ (fs)	10	27	63	74	128	53	−561

4. 2.00–2.09 eV

The next energy region of interest which shows much structure in Figs. 2 and 5 is that between 2.00 and 2.09 eV. In Fig. 2, $P_{00}^{R}(total)$ and $P_{00}^{R}(3)$ peak at about 2.06 eV, and $P_{00}^{R}(2)$ peaks a bit earlier at about 2.04 eV.

Argand diagrams plotted in this energy range are presented in Figs. 11, 12, and 13. In Fig. 11, for transitions into HF ($v_f = 2$, $j_f = 9$–12), all four diagrams are qualitatively similar. The energy trajectories start at 1.83 eV and swirl smoothly until reaching about 2.03 eV. The trajectories then head nearly straight towards the origin (or parallel to this path) which gives each diagram a "lobe-like" shape. These lobes are indicative of these transitions participating weakly with a broad resonance. We also note that the Argand diagrams for HF ($v_f = 2, j_f = 8$, 13–15) look qualitatively similar on this energy range.

In Fig. 12, the diagrams for the transitions into HF ($v_f = 3$, $j_f = 0$–3) are also all qualitatively similar. Each diagram possesses a lobe around 2.03 eV, although these lobes are not as prominent as those in the HF ($v_f = 2$) transitions in Fig. 11. Also shown are Argand diagrams for two nonreactive transitions in Fig. 13. These each exhibit a lobe around 2.03 eV which is somewhat similar to that observed in Fig. 11. The behavior of the diagrams in Figs. 11, 12, and 13 suggest that all of these transitions are participating in a broad resonance.

A more compelling piece of evidence for the existence of a resonance on this energy range is the behavior exhibited by the time delays in Figs. 14(a) and 14(b). In Fig. 14(a), the curves plotted for the transitions into HF ($v_f = 3$) states show a first derivative-like behavior centered about 2.04 eV. That is, the time delay dips before 2.04 eV and then monotonically and steeply increases through about 2.04 eV and then reaches a maximum after 2.04 eV. The time delays in Fig. 14(b) for the transitions into HF $v_f = 2$ states also exhibit this derivative behavior centered at about 2.05–2.06 eV. Another curious feature is that the curves in Fig. 14(b) peak *then* dip in the derivative region in contrast to the dip *then* peak in Fig. 14(a). An attempt has been made to place a physical interpretation of this derivative behavior to possibly extract an estimate of a lifetime from these curves. We have come to the conclusion that the position in *energy* at which a resonance occurs can be obtained from the behavior of the time delay (oscillation or deviation with respect to the back-

ground) but an absolute value of the lifetime can not be extracted. A similar conclusion can be formed based on the work of Hipes and Kuppermann[41] for resonances in the $H + H_2$ system.

To actually obtain an estimate of the lifetime, the eigenlifetimes of the collision lifetime matrix in this energy region were examined. The data in Table V indicate the existence of a resonance near 2.045 eV with a lifetime of ≈ 35 fs which involves states which correlate with H_2 ($v = 0$, j = 0,2 and 4) and HF ($v = 3, j = 1,2$, and 3) states. Again, the absolute accuracy of such a short lifetime we estimate to be $\pm$ 10% due to the numerical fit of the $d\mathbf{S}/dE$ matrix.

As apparent in Fig. 5, the H_2 states ($v = 0, j = 0$, 2 and 4) are also involved in this resonance. $P_{00}^{NR}(0,0)$ and $P_{00}^{NR}(0,2)$ plunge to nearly zero at about 2.055 eV whereas $P_{00}^{NR}(0,4)$ is sharply peaked at about 2.04 eV.

In summary, the broad resonance at about 2.06 eV is due to an efficient coupling between the product HF $v = 2$ and 3 states with the reactant H_2 ($v = 0$) states. A possible physical mechanism for this coupling is discussed later in conjunction with the reduced dimensionality results.

5. 2.09–2.10 eV

The sharp dip in $P_{00}^{R}(total)$ and $P_{00}^{R}(3)$ and the sharp peak in $P_{00}^{R}(2)$, all at about 2.095 eV in Fig. 2(a) are all due to a closed channel resonance as HF ($v = 4, j = 0$) opens at 2.0914 eV. [Note how steeply $P_{00}^{R}(4)$ increases from the threshold at 2.0914 eV in Fig. 2(a)].

This resonance shows up quite succinctly in the Argand diagrams plotted in Fig. 11. After the energy trajectory travels through the origin near 2.05 eV it attempts to swirl smoothly again when it *suddenly* makes a tight loop at about 2.095 eV. (There are ten calculated points between 2.09 and 2.10 eV). The loops circulate in a *counter*clockwise direction; i.e., $d\phi/dE$ is *positive* for each of these transitions. A loop in the Argand diagram at about 2.095 eV is also observed for the transitions $f =$ HF ($v = 2$, $j = 8$–14), although these are not presented. The implication of these loops indicates that *all* of these final states are participating quite strongly with this closed channel resonance.

The resonance does not appear as dramatically in the Argand diagrams for transitions to the HF ($v_f = 3, j_f = 0$–3) states as shown in Fig. 12. In all four of these transitions, the resonance is indicated by a depression (concave outward) at around 2.095 eV on an energy trajectory which is otherwise "normal" (concave inward towards the origin). Yet, the path which is concave outward suggests that the trajectory on this portion is a circle centered at a point other than the origin. The circulation of an Argand diagram about a point other than the origin signifies the existence of a resonance.

The Argand diagrams of the nonreactive transitions into H_2 ($v_f = 0, j_f = 0$ and 2) in Fig. 13 exhibit a cusp at about 2.095 eV. This cusp indicates that $d\phi/dE$ for these transitions is behaving in a resonant fashion.

This resonance can also be seen in the time delays presented in Figs. 14(a) and 14(b). In Fig. 14(a), the HF $v_f = 3$ transitions show a sharp dip centered at about 2.095 eV, whereas in Fig. 14(b), the HF $v_f = 2$ transitions show a sharp peak centered at about 2.095 eV. Again the absolute value of these peaks or dips are not significant with respect to providing an absolute estimate of a lifetime. These curves *do* indicate that these HF states are participating in this resonance at an energy of about 2.095 eV.

The eigenlifetimes of the collision lifetime matrix were examined for this energy range. At 2.092 and 2.093 eV, eigenlifetimes of 134 and 80 fs, respectively, were obtained whose eigenvectors were mixtures of HF (v, j = 0) states in the ratio ($v = 4$:3:2) of 350:25:1 and 33:30:1, respectively. At a slightly higher energy, the data in Table VI indicate a resonance of lifetime ≈ 128 fs which correlates with the HF ($v = 4$, $j = 0$) state, HF ($v = 3$) states and H_2 ($v = 0$) states. Curiously, the eigenvalue of this particular mixture of states becomes extremely negative ($-$ 561 fs) at 2.099 eV. Having seen this type of behavior at other energies, we believe possibly that the lifetime is extremely negative due to a threshold, such as that for HF ($v = 4, j = 1$) at 2.096 eV. However, this apparent "instability" in the lifetimes may be correlated with the accuracy of the numerical S matrix derivatives. Again, a direct calcualtion[40] of these derivatives could clarify this situation.

The nonreactive probabilities presented in Fig. 5 also indicate that the H_2 ($v = 0$) states are participating in the resonance as $P_{00}^{NR}(v_f = 0, j)$ for $j = 0, 2, 4$, and 6 all exhibit a sharp peak in the energy region around 2.095 eV.

6. 2.10–2.25 eV

In Fig. 2(a), we tentatively attribute the broad dip in $P_{00}^{R}(total)$, $P_{00}^{R}(3)$, and $P_{00}^{R}(4)$ centered at about 2.16 eV to a threshold resonance due to the opening of the H_2 ($v = 1$, $j = 0$) state at 2.1589 eV. Argand diagrams for some transitions that have been plotted in this energy region (which are not shown) exhibit behavior indicative of a resonance.

B. Eigenphase sums

We also looked at the eigenphase sum at various total energies. The set of eigenphases $\{\delta_n(E)\}$ are defined[42] by the unitary transformation U which diagonalizes $S(E)$

$$U^{\dagger}S(E)U = \exp[2i\boldsymbol{\delta}(E)], \tag{50}$$

where $\boldsymbol{\delta}(E)$ is the vector with components $\{\delta_q(E)\}$. The maximum value of q is dictated by the number of open channels in $S(E)$ at the energy E. The eigenphase sum is then constructed as

$$\Delta(E) = \sum_q \delta_q(E). \tag{51}$$

For multichannel processes (inelastic electron–atom and electron–molecule scattering) it has been observed empirically[42] that $\Delta(E)$ increases by π as E passes through a resonance, although this has not been proven rigorously. It is well known that the phase shift for an isolated single channel resonance increases by π as E passes through a resonance.

To obtain an estimate of how quickly $\Delta(E)$ varies as a function E, $S(E)$ was calculated at 0.0001 eV intervals starting at 1.89 eV. This energy was chosen in a region where we believe no resonances are occurring as we wanted an esti-

TABLE VII. Eigenphase sums $\Delta(E)$. Order of $S(E)$ matrix = 153.

E (eV)	$\Delta(E)$ (radian)	$\frac{d\Delta(E)}{dE}$ (radian/eV)
1.8900	3.313 28	
		7142
1.8901	2.599 11	
		7148
1.8902	1.884 35	
		7147
1.8903	1.169 64	
		7147
1.8904	0.454 98	

mate of only the smoothly varying background contribution to $\Delta(E)$. In Table VII $\Delta(E)$ and $d\Delta(E)/dE$ are presented as a function of E. $d\Delta(E)/dE$ was determined by a two-point finite difference. Using the average of $d\Delta(E)/dE$ from Table VII, an estimate can be made of how much $\Delta(E)$ changes for a given energy increment. If $\Delta E = 0.01$ eV, which is typical [see Table III], then the change in $\Delta(E)$ is

$$\frac{d\Delta(E)}{dE}\Delta E \approx 23\pi \text{ radian.} \tag{52}$$

To find a possible resonance near this energy with this approach, a shift in $\Delta(E)$ by π would have to be detected within a background $\Delta(E)$ which changes by 23π over an interval of just 0.01 eV! This detection is probably not possible.

C. Comparison with reduced dimensionality results

In Figs. 16(a) and 16(b) reaction probabilities for the $F + H_2$ reaction on the T5A PES are presented which were calculated[43] with a collinear (1D) and the BCRLM (approximate 3D, reduced 3D) approach, respectively. The accurate 3D results in Fig. 2(a) share many similar features with those given in Figs. 16(a) and 16(b). The HF $v_f = 2$ resonance near the total reaction threshold appears both in the 1D and BCRLM calculations. This resonance in 1D, which occurs at 1.663 55 eV, is very narrow (of width $\approx 1 \times 10^{-4}$ eV). Both the 1D and BCRLM results show a resonance at 1.99 and 2.055 eV, respectively, which is likely caused by the same mechanism which yielded the resonance in full 3D near 2.06 eV in Fig. 2(a). The difference between the location of this resonance in 1D, reduced 3D, and full 3D is probably due to the manner in which the zero point energy for the bending motion of the three atom system is included. In 1D, the bending motion in neglected; in reduced 3D, the bending is included approximately; and in full 3D, the bending is treated exactly. Furthermore, the appearance of this resonance in reduced dimensions suggests that it may be explained using a periodic orbit[44] argument. That is, in terms of semiclassical dynamics, a trajectory may become snarled and trapped on the effective PES for a given value of total angular momentum due to the existence of vibrationally adiabatic barriers.

All three types of calculations share similar features near the occurence of the HF $v_f = 4$ threshold. This threshold is barely discernible in 1D near 2.09 eV in Fig. 16(a) and shows distinctly in the BCRLM calculations in Fig. 16(b) at about 2.105 eV. Also in the BCRLM calculations, the $v_f = 3$ reaction probability shows a slight depression at 2.10 eV, whereas in full 3D $P_{00}^{R}(3)$ in Fig. 2(a) shows a sharp dip near the $v_f = 4$ threshold.

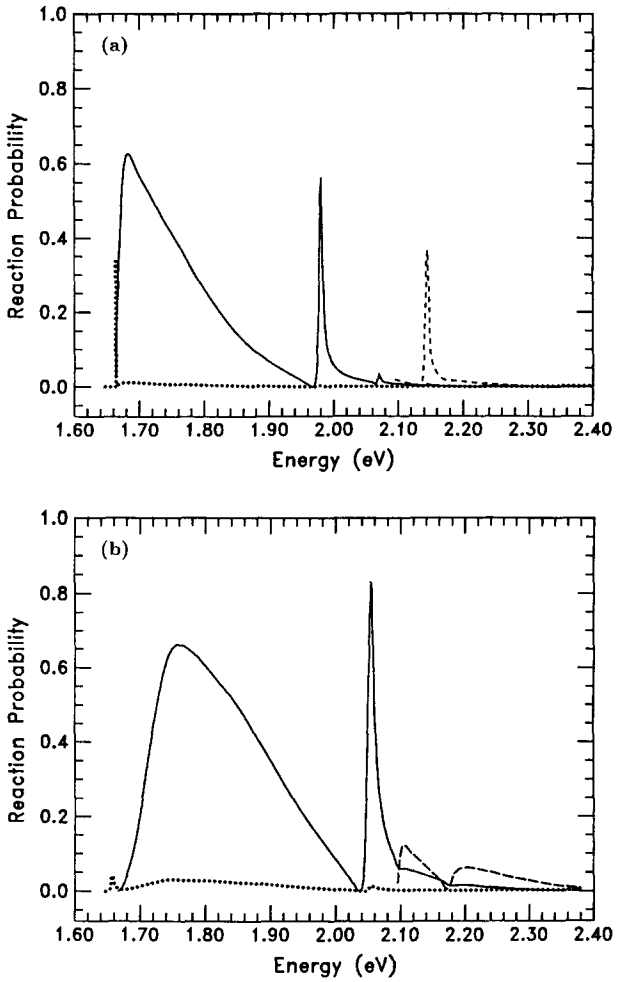

FIG. 16. (a) Collinear (1D) $F + H_2$ reaction probabilities $P_{v_i=0}(v_f)$ plotted vs total energy. Legend: (dots) $v_f = 2$; (solid line) $v_f = 3$; (dashed line) $v_f = 4$. (b) BCRLM $F + H_2$ reaction probabilities $P_{v_i=0}(v_f)$ plotted vs total energy for zero ($L = 0$) angular momentum. Same Legend as (a).

The largest contrast between the results in Fig. 2(a) and those in Figs. 16(a) and 16(b) is the behavior of the $v_f = 3$ reaction probability over the range 1.68–1.95 eV. Both the 1D and BCRLM probabilities rise quickly, achieve a maximum, and then smoothly decrease to zero. The 3D $v_f = 3$ probability looks like the 1D and BCRLM counterparts *except* that some probability has been removed or scooped out centered at about 1.80 eV. Most of this removed reaction probability appears in the reactant channel as an enhancement of the inelastic probability to form H_2 ($v = 0, j = 2$). (See Fig. 5.) The absence of this feature in 1D and in the BCRLM calculations and the strong involvement of the H_2 ($v = 0, j = 2$) state in the 3D calculations suggest that the flow of flux into the inelastic channel is due to a coupling of *rotational* diatomic fragment states, a coupling which is omitted in the 1D and BCRLM approaches. Also, the opening of the H_2 ($v = 0, j = 4$) state at 1.791 eV may also be playing a crucial role in the dynamics.

VI. CONCLUSIONS

We presented accurate 3D, full CC, $J = 0$ calculations for the $F + H_2$ reaction using the realistic T5A PES. The adiabatic surface function basis was generated using the DVR method. We outlined the DVR method, derived the necessary matrix elements and demonstrated the convergence of the surface functions. From the analysis of the reaction probabilities, both into final v_f and final j_f states, we correlated much of the observed structure with plausible explanations concerning dynamical resonances. To aid in the evaluation of the resonance and quantum structure, we also analyzed the phases of the S matrices, Argand diagrams, time delays and eigenlifetimes of the collision lifetime matrix. From this analysis we were able to identify the following: (1) a closed channel [HF ($v = 3$)] resonance at 1.6625 eV; (2) a quantum feature around 1.80 eV which involves the $v = 2$ and 3 states of HF and the $v = 0, j = 2$ state of H_2; (3) a strong broad resonance at 2.06 eV which involves $v = 2$ and 3 states of HF and $v = 0$ states of H_2; (4) a *narrow* closed channel [HF ($v = 4$)] resonance at 2.095 eV which involves the HF $v = 2$, 3 and 4 channels as well as the $v = 0$ channels of H_2; and (5) a possible resonance at 2.16 eV due to the opening of the H_2 $v = 1$ channel. Although we have provided an extensive analysis of the $J = 0$ results, future work is necessary to generate $J \neq 0$ information to construct DCSs and compare directly with experiment. It will be interesting to see how the resonance features evolve as J is increased to nonzero values.

ACKNOWLEDGMENTS

We thank R. M. Whitnell and J. C. Light for sending us their 2D DVR surface function code. We thank E. F. Hayes and R. B. Walker for many helpful discussions, for providing the code for fitting the S matrix phases, and for generating the collinear and BCRLM results. This work was performed under the auspices of the U.S. Department of Energy and was also supported in part by the National Science Foundation under Grant No. CHE-8706385.

[1] J. H. Parker and G. C. Pimentel, J. Chem. Phys. **51**, 91 (1969).
[2] J. C. Polanyi and K. B. Woodall, J. Chem. Phys. **57**, 1574 (1972).
[3] D. M. Neumark, A. M. Wodtke, G. N. Robinson, C. C. Hayden, and Y. T. Lee, *Resonances in Electron–Molecule Scattering, Van der Waals Complexes, and Reactive Chemical Dynamics*, edited by D. G. Truhlar, ACS Symposium Series 263 (Am. Chem. Soc., Washington, D.C., 1984), p. 479; J. Chem. Phys. **82**, 3045 (1985).
[4] J. T. Muckerman, Theoretical Chem. Advan. Perspect. A **6**, 1 (1981).
[5] G. C. Schatz, J. M. Bowman, and A. Kuppermann, J. Chem. Phys. **58**, 4023 (1973); S. F. Wu, B. R. Johnson, and R. D. Levine, Mol. Phys. **35**, 3501 (1973).
[6] Y. Shan, B. H. Choi, R. T. Poe, and K. T. Tang, Chem. Phys. Lett. **57**, 378 (1978).
[7] M. J. Redmon and R. E. Wyatt, Intern. J. Quantum Chem. Symp. **9**, 403 (1975); Chem. Phys. Lett. **63**, 209 (1979).
[8] M. Baer, J. Jellinek, and D. J. Kouri, J. Chem. Phys. **78**, 2962 (1983); Z. H. Zhang, N. Abusalbi, M. Baer, D. J. Kouri, and J. Jellinek, *Resonances in Electron–Molecule Scattering, van der Waals Complexes, and Reactive Chemical Dynamics*, edited by D. G. Truhlar, ACS Symposium Series 263 (Am. Chem. Soc., Washington D. C., 1984), p. 457.
[9] E. F. Hayes and R. B. Walker, *Resonances in Electron–Molecule Scattering, van der Waals Complexes, and Reative Chemical Dynamics*, edited by D. G. Truhlar, ACS Symposium Series 263 (Am. Chem. Soc., Washington, D.C., 1984), p. 493; J. Chem. Phys. **88**, 5978 (1988); **89**, 5598 (1988).
[10] J. Z. H. Zhang and W. H. Miller, J. Chem. Phys. **88**, 4549 (1988); **90**, 7610 (1989).
[11] C-h. Yu, Y. Sun, D. J. Kouri, P. Halvick, D. G. Truhlar, and D. W. Schwenke, J. Chem. Phys. **90**, 7608 (1989).
[12] R. Steckler, D. G. Truhlar, B. C. Garrett, N. C. Blais, and R. B. Walker, J. Chem. Phys. **81**, 5700 (1984).
[13] F. B. Brown, R. Steckler, D. W. Schwenke, D. G. Truhlar, and B. C. Garrett, J. Chem. Phys. **82**, 188 (1985).
[14] R. Steckler, D. G. Truhlar, and B. C. Garrett, J. Chem. Phys. **82**, 5499 (1985).
[15] D. W. Schwenke, R. Steckler, F. B. Brown, and D. G. Truhlar, J. Chem. Phys. **84**, 5706 (1986); **86**, 2443 (1987).
[16] C-h. Yu, D. J. Kouri, M. Zhao, D. G. Truhlar, and D. W. Schwenke, Chem. Phys. Lett. **157**, 491 (1989).
[17] J. D. Kress, Z. Bačić, G. A. Parker, and R. T Pack, Chem. Phys. Lett. **157**, 484 (1989).
[18] C-h. Yu, D. J. Kouri, M. Zhao, D. G. Truhlar, and D. W. Schwenke, Int. J. Quantum Chem. Symp. (in press).
[19] J. C. Light, I. P. Hamilton, and J. V. Lill, J. Chem. Phys. **82**, 1400 (1985).
[20] R. T Pack and G. A. Parker, J. Chem. Phys. **87**, 3888 (1987).
[21] G. A. Parker, R. T Pack, B. J. Archer, and R. B. Walker, Chem. Phys. Lett. **137**, 564 (1987).
[22] T. Ericsson and A. Ruhe, Math. Comput. **35**, 1251 (1980).
[23] S. Padkjaer and J. D. Kress (unpublished results).
[24] B. R. Johnson, J. Chem. Phys. **67**, 4086 (1977); **69**, 4678 (1978).
[25] I. P. Hamilton and J. C. Light, J. Chem. Phys. **84**, 306 (1986).
[26] Z. Bačić, R. M. Whitnell, D. Brown, and J. C. Light, Comput. Phys. Comm. **51**, 35 (1988).
[27] Z. Bačić and J. C. Light, Annu. Rev. Phys. Chem. **40**, 469 (1989).
[28] Z. Bačić and J. C. Light, J. Chem. Phys. **85**, 4594 (1986).
[29] J. C. Light and Z. Bačić, J. Chem. Phys. **87**, 4008 (1987).
[30] Z. Bačić and J. C. Light, J. Chem. Phys. **86**, 3065 (1987).
[31] Z. Bačić, D. Watt, and J. C. Light, J. Chem. Phys. **89**, 947 (1988).
[32] R. M. Whitnell and J. C. Light, J. Chem. Phys. **90**, 1774 (1989).
[33] R. M. Whitnell and J. C. Light, J. Chem. Phys. **89**, 3674 (1988).
[34] G. A. Parker, R. T Pack, A. Laganà, B. J. Archer, J. D. Kress, and Z. Bačić, in *Supercomputer Algorithms for Reactivity, Dynamics and Kinetics of Small Molecules*, edited by A. Laganà (Kluwer, Dordrecht, 1989), p. 105.
[35] J. D. Kress, G. A. Parker, R. T Pack, B. J. Archer, and W. A. Cook, Comput. Phys. Comm. **53**, 91 (1989).
[36] J. D. Kress, Z. Bačić, G. A. Parker, and R. T Pack (in preparation).
[37] R. B. Walker (unpublished).
[38] F. T. Smith, Phys. Rev. **118**, 349 (1960).
[39] A. Kuppermann, in *Potential Energy Surfaces and Dynamics Calculations*, edited by D. G. Truhlar (Plenum, New York, 1981), p. 375.
[40] E. F. Hayes and R. B. Walker, Chem. Phys. Lett. **151**, 537 (1988); J. Chem. Phys. **91**, 4106 (1989).
[41] P. G. Hipes and A. Kuppermann, Chem. Phys. Lett. **133**, 1 (1987).
[42] A. Hazi, Phys. Rev. A **19**, 920 (1979).
[43] R. B. Walker (private communication).
[44] E. Pollak and P. Pechukas, J. Chem. Phys. **69**, 1218 (1978); E. Pollak and M. S. Child, Chem. Phys. **60**, 23 (1981).